Geochemistry Geophysics Geosystems G3
AN ELECTRONIC JOURNAL OF THE EARTH SCIENCES
Published by AGU and the Geochemical Society

Article
Volume 7, Number 4
12 April 2006
Q04003, doi:10.1029/2005GC001038
ISSN: 1525-2027

The Cleft revealed: Geologic, magnetic, and morphologic evidence for construction of upper oceanic crust along the southern Juan de Fuca Ridge

Debra S. Stakes
Monterey Bay Aquarium Research Institute, 7700 Sandholdt Road, Moss Landing, California 94039-9644, USA

Now at Division of Science and Environmental Policy, California State University Monterey Bay, Building 53/E318, Monterey, California 93955, USA (debra_stakes@csumb.edu)

Michael R. Perfit
Department of Geological Sciences, University of Florida, Gainesville, Florida 32611-2120, USA

Maurice A. Tivey
Department of Geology and Geophysics, Woods Hole Oceanographic Institution, Woods Hole, Massachusetts 02543, USA

David W. Caress
Monterey Bay Aquarium Research Institute, 7700 Sandholdt Road, Moss Landing, California 94039-9644, USA

Tony M. Ramirez and Norman Maher
Monterey Bay Aquarium Research Institute, 7700 Sandholdt Road, Moss Landing, California 94039-9644, USA

Now at Marine Geoscience Division, AOA Geophysics, 7532 Sandholdt Road, Moss Landing, California 95039, USA.

[1] The geology and structure of the Cleft Segment of the Southern Juan de Fuca Ridge (JdFR) have been examined using high-resolution mapping systems, observations by remotely operated vehicle (ROV), ROV-mounted magnetometer, and the geochemical analysis of recovered lavas. Bathymetric mapping using multibeam (EM300) coupled with in situ observations that focused on near-axis and flank regions provides a detailed picture of 0 to 400 ka upper crust created at the southern terminus of the JdFR. A total of 53 rock cores and 276 precisely located rock or glass samples were collected during three cruises that included sixteen ROV dives. Our observations of the seafloor during these dives suggest that many of the unfaulted and extensive lava flows that comprise and/or cap the prominent ridges that flank the axial valley emanate from ridge parallel faults and fissures that formed in the highly tectonized zone that forms the walls of the axial valley. The geochemically evolved and heterogeneous nature of these near-axis and flank eruptions is consistent with an origin within the cooler distal edges of a crustal magma chamber or mush zone. In contrast, the most recent axial eruptions are more primitive (higher MgO), chemically homogeneous lobate, sheet, and massive flows that generate a distinct magnetic high over the axial valley. We suggest that the syntectonic capping volcanics observed off-axis were erupted from near-axis and flank fissures and created a thickened extrusive layer as suggested by the magnetic and seismic data. This model suggests that many of the lavas that comprise the elevated ridges that bound the axial valley of the Cleft Segment were erupted during the collapse of a magmatic cycle not during the robust phase that established a new magmatic cycle.

Components: 19,228 words, 20 figures, 3 tables, 1 dataset.

Keywords: basalt; ridge.

Index Terms: 3045 Marine Geology and Geophysics: Seafloor morphology, geology, and geophysics; 3614 Mineralogy and Petrology: Mid-oceanic ridge processes (1032, 8416); 3641 Mineralogy and Petrology: Extrusive structures and rocks.

Received 9 June 2005; **Revised** 15 September 2005; **Accepted** 28 December 2005; **Published** 12 April 2006.

Stakes, D. S., M. R. Perfit, M. A. Tivey, D. W. Caress, T. Ramirez, and N. Maher (2006), The Cleft revealed: Geologic, magnetic, and morphologic evidence for construction of upper oceanic crust along the southern Juan de Fuca Ridge, *Geochem. Geophys. Geosyst.*, *7*, Q04003, doi:10.1029/2005GC001038.

1. Introduction

[2] The Cleft Segment of the southern Juan de Fuca Ridge (JdFR) is a highly symmetrical intermediate-rate spreading center (~6 cm/yr full rate) with a well-defined axial valley cut by the 30–90 m wide, 10–15 m deep, "cleft" that extends 10 km down the center of the axial valley (Figures 1 and 2) [*Normark et al.*, 1986, 1987]. The "cleft" is an axial collapse trough that is morphologically (and perhaps genetically) identical to the axial summit collapse trough (ASCT) described for the East Pacific Rise (EPR) [*Fornari et al.*, 1998]. The primary difference between the "cleft" and an EPR ASCT is that the "cleft" is in the center of an axial valley rather than at the summit of an axial high. The axial valley of the Cleft Segment has other morphologic and volcanic features similar to those documented on the magmatically robust northern EPR [*Normark et al.*, 1986, 1987; *Embley et al.*, 1991; *Embley and Chadwick*, 1994; *Perfit and Chadwick*, 1998]. Recent volcanism and active high-temperature hydrothermal sites are concentrated in a narrow <100 m wide zone around the "cleft" [*Normark et al.*, 1983]. The cleft has erupted lobate, sheet and massive flows probably just prior to the last two decades of observation [*Normark et al.*, 1987; *Embley et al.*, 1991; *Embley and Chadwick*, 1994]. North and south of the area with a central "cleft," the axial morphology changes to a more subdued axial valley dominated by thick, linear, pillow mounds; features similar to the axial volcanic ridges (AVR) common on slow spreading ridges [*Chadwick and Embley*, 1994; *Smith*, 1999; *Head et al.*, 1996]. The volcanically and hydrothermally active axial valley is similar, although not identical to, the axial rift valleys or graben of slow spreading centers. The axial valley is bounded by 75–200 meter high "bow-form" ridges, postulated as vestiges of split, axial volcanoes (Figure 2) [*Kappel and Ryan*, 1986]. These "split ridges" are suggested to delineate periods of robust axial volcanism followed by periods of tectonic extension. Such large constructional features are smaller in scale than the "thermal bulge" axial topographic highs of fast spreading ridges [*Carbotte and Macdonald*, 1994]. Thus, according to the split volcano hypothesis, most of the magmatism at the Cleft Segment occurs at the axis, with cyclic oscillations between robust volcano building and waning periods of largely amagmatic faulting, extension and disruption.

[3] The largely symmetrical and structurally simple southern Juan de Fuca Ridge was created as a result of a tectonically complex history of propagating rifts and changes in plate motion associated with the breakup and subduction of the Farallon plate beneath North America [*Wilson*, 1988; *Wilson et al.*, 1984]. On the basis of the youngest magnetic anomaly patterns, the southward propagation of the southernmost Juan de Fuca ceased approximately 1.4 m.y. B.P. with abrupt terminations at the Blanco Transform Zone (BTZ) [*Embley and Wilson*, 1992]. The BTZ has undergone several northward jumps at this intersection in concert with the conjugate processes of rift propagation and failure. *Embley and Wilson* [1992] suggest that the most recent readjustment was a northward jump at approximately 0.4 million years ago that has offset the Brunhes and Jaramillo magnetic anomalies across the West Blanco Deep. The current morphology of the ridge-transform intersection (RTI) is similar to RTIs on the EPR with the inside corner perturbed by the propagator (the eastern pseudofault) more than 50 km east of the ridge axis. However, unlike many intersections on the EPR where the ridge axis gradually deepens as it bends into the transform domain, the western RTI is characterized by an abrupt termination of the BTZ against a hummocky and inflated ridge crest that overshoots and hooks around the deep transform to the south (Figure 3).

[4] With an average spreading rate of 5.6 cm/year [*Wilson*, 1992], the 25 km wide by 70 km long section of oceanic crust described here (Figure 1) represents the cumulative effects of crustal accretion during the last ~400 kyr, and as such, entirely

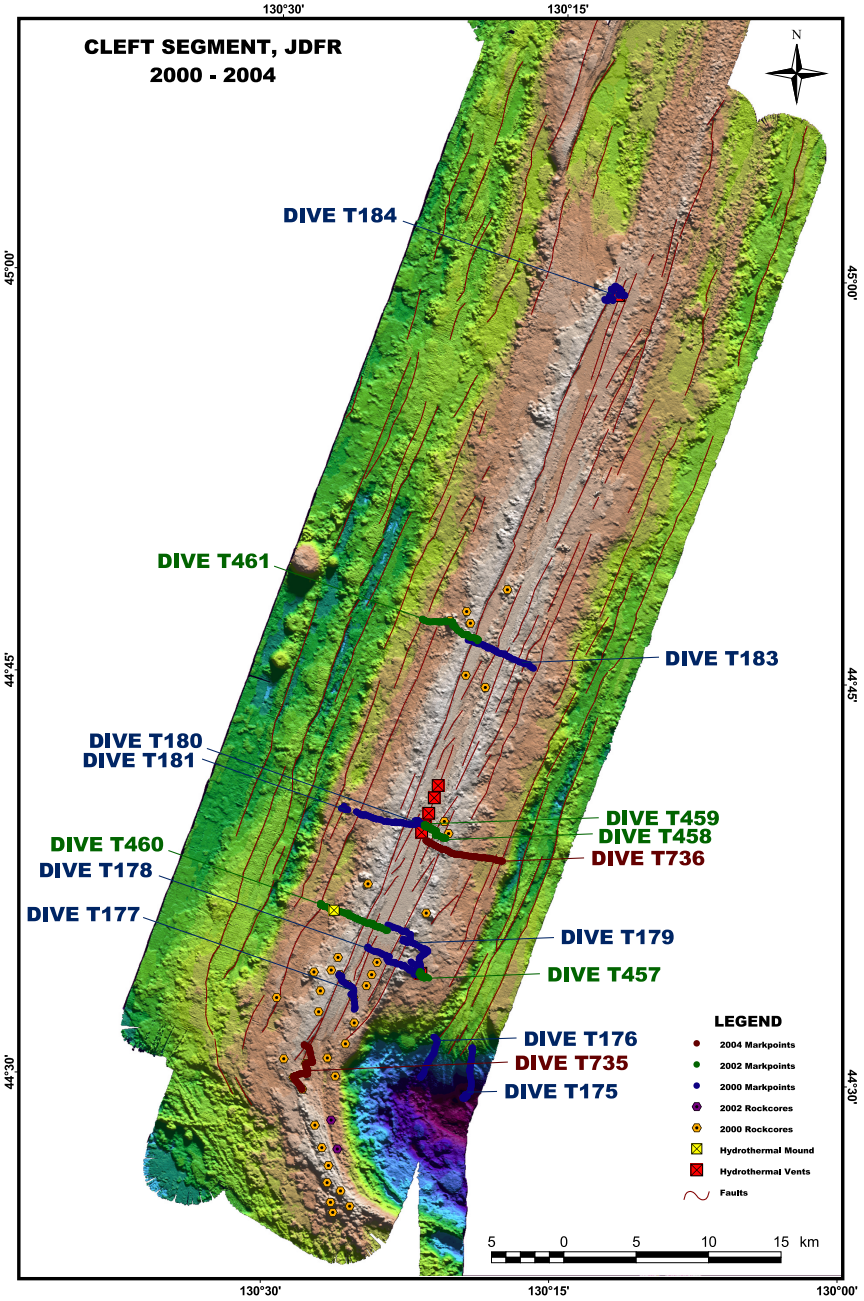

Figure 1. Shaded relief bathymetry of the entire south Cleft Segment derived from Simrad EM300 sonar data. This figure includes all the dive tracks for the ROV *Tiburon* from the July 2000 to August 2004 field programs. Bathymetric data is available from MBARI as Digital Data Series 7. The Cleft Segment overlaps with the Vance segment in the northern part of the figure and intersects the Blanco Transform Fault in the south. Red squares with crosses denote known high-temperature vent sites, and yellow squares with crosses are low-temperature vent sites. Yellow and purple hexagons are locations of rock core glass samples. Blue, green, and burgundy dots denote samples/observation points from the 2000, 2002, and 2004 ROV dive series, respectively. Major faults are shown as brown lines. Maps showing sample numbers and summary of framegrabs and dive observations are provided as auxiliary material to this paper.

postdates the complexities of rift propagation. The age of the crust is also well-constrained by in situ measurements of outcrop magnetization used to identify the Brunhes/Matuyama and Jaramillo polarity transitions exposed on the north wall of the West Blanco Deep, ~24 km from the spreading axis [*Tivey et al.*, 1998]. This study also documents that the lavas of the upper portion of the extrusive

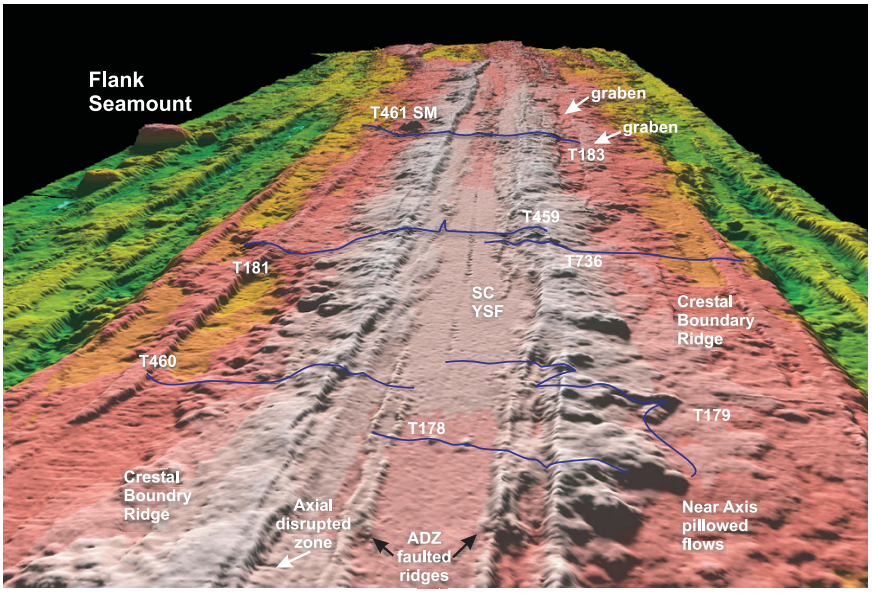

Figure 2. Shaded relief image of the Cleft Segment looking from the south to the north, highlighting the crestal boundary ridges, the axial disrupted zone (ADZ), and the neovolcanic zone within the axial valley. Note the "cleft" is apparent as a thin linear fissure that bisects the axis in the shoalest portion of the segment. The smooth axial floor around the cleft marks the distribution of the South Cleft young sheet flows (SC YSF). The high-temperature active vents are all within the cleft fissure within the shoalest area. ROV dives T178, T179, T181, T460, and T736 ascended the eruptive edifices that comprise the "bowform" or Crestal Boundary Ridge (CBR) of the South Cleft Segment. ROV dives T183 and T461 crossed the Cleft center segment where the axis floor is characterized by pillowed flows rather than sheet flows. Note the flank grabens on the eastern side and the flank seamounts on the western side. All of the unannotated shaded relief images are provided in the auxiliary material to this paper.

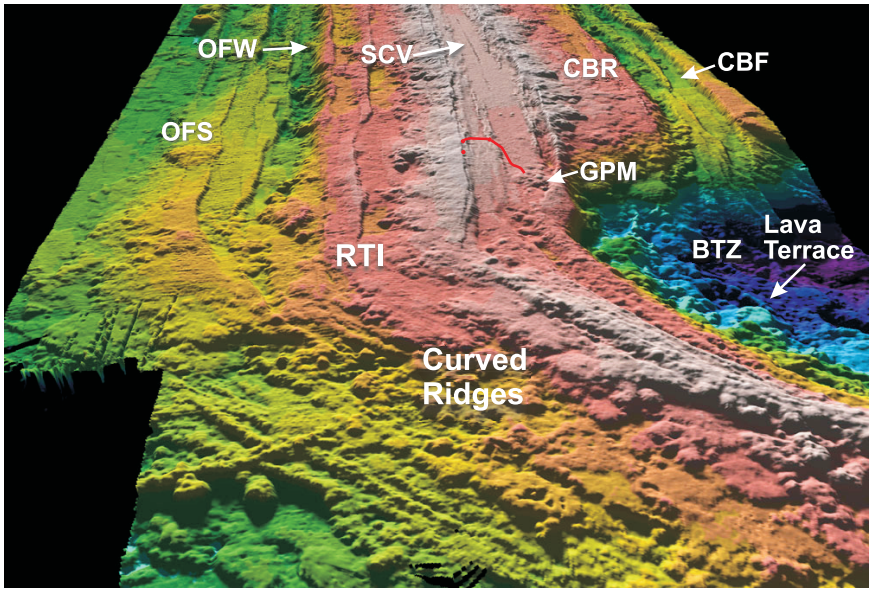

Figure 3. Shaded relief perspective of the Blanco Transform Zone (BTZ) at the ridge-transform intersection (RTI) looking to the north. Note the pillowed flows that drape the northern wall of the BTZ and the walls of the curved ridges that wrap around and define the RTI. A large ponded lava terrace on this wall is identified. The locations of the south Cleft vents (SCV), curved basement faults (CBF), giant andesitic pillow mounds (GPM), oblique fault segments (OFS), and outward facing wall (OFW) are shown.

layer extend several kilometers away from the spreading axis, which has implications for the width of the crustal accretion zone [*Tivey et al.*, 1998].

[5] In this paper we report the results of our geologic, morphologic and magnetic investigations of the Cleft Segment during cruises in 2000, 2002 and 2004. These investigations concentrated on off-axis regions that have never been studied before in an attempt to relate recent high-resolution mapping and geophysical results to fine-scale observations, sampling and magnetic measurements made by remotely operated vehicle (ROV). The overall objectives of our study are to present an integrated picture of this well-known intermediate spreading-rate ridge segment and to provide additional constraints on the construction and development of the uppermost crust of the Cleft Segment during the past 400 kyr.

2. Methods

[6] During 1998 the entire Cleft Segment was surveyed (Figure 1) using a hull-mounted 30 kHz Simrad EM300 multibeam sonar. With 2 degree by 2 degree beam resolution, the EM300 achieved a ~30 m lateral resolution over a 3 km swath width. The swath data were processed using the MB-System software package [*Caress and Chayes*, 1996; 2005]. Gridded bathymetry and mosaicked backscatter are available from MBARI [*MBARI Mapping Team*, 2001], and all of the swath data are available from the National Geophysical Data Center at http://www.ngdc.noaa.gov/.

[7] The mapping program was followed by a series of in situ observations made from the ROV *Tiburon* operated from the Research Vessel Western Flyer during July 2000 and August 2002 and 2004. A total of 16 ROV dives were completed across the Cleft spreading center ranging from (north to south): one dive at North Cleft (T184), two dives in the segment center (T183; T461), five dives across the axis near the South Cleft hydrothermal fields (T180-T181; T458-T459; T736); five dives on the southernmost part of the segment (T177, T178, T179, T457, T460), two dives on the northern wall of the intersection with the Blanco Fracture Zone (T175-T176) and one dive on the hooked ridges that define the western side of the nodal basin (T735) (Figures 1, 2, and 3). A detailed sampling program was carried out as part of the ROV and surface ship operations. Typically, between 20 and 40 lava and glass samples were recovered (with the manipulator and small wax cores respectively) on each ROV dive. Wax rock cores were also taken from the ship at an additional 53 locations in order to extend the sampling coverage to areas not visited by ROV. In addition to the visual observations and geologic sampling, a 3-axis magnetometer (Honeywell HMR2300 magnetoresistor) mounted onto Tiburon collected magnetic field data along the ROV dive tracks. The ROV observations, contemporaneous magnetic field measurements, digital still and video images and geologic sampling were all located with respect to the EM300 bathymetry through a real-time ArcView-based navigation and GIS system using the EM300 bathymetric basemap. The bathymetric data, ship locations and ROV USBL (ultra-short baseline) navigation used a common GPS datastream with real-time depth (from the ROV) providing consistent position information within 10–20 meters of bathymetric features on the EM300 bathymetry.

[8] Glasses from the cores and outer rinds of lavas were analyzed for major and minor elements by electron microprobe at the USGS in Denver and Florida International University in Miami using a JEOL Superprobe (maps of sample locations and major element compositions of glasses are available as auxiliary material; see 2005gc001038-fs01.eps to 2005gc001038-fs05.eps and 2005gc001038-ts01.txt, respectively). Individual glass analyses were corrected for any temporal or interlaboratory bias by normalizing the measured values to accepted values of in-house secondary glass standards JdF-D2 and 2392-9 [see *Smith*, 1999]. Using this method we have found excellent agreement between samples analyzed in this study and those analyzed at the USGS in Menlo Park [e.g., *Eaby et al.*, 1984; *Dixon et al.*, 1986] over the past 20 years. The entire geochemical data set (including trace elements and isotopes), petrologic information and discussion of the petrogenesis of the S. Cleft suite are the subjects of another paper (M. R. Perfit et al., manuscript in preparation, 2006).

3. Regional Features Observed With High-Resolution Bathymetric and Backscatter Data

[9] The spreading axis is characterized by a well-defined axial valley or axial graben [*Carbotte et*

[1] Auxiliary material is available at ftp://ftp.agu.org/apend/gc/2005gc001038.

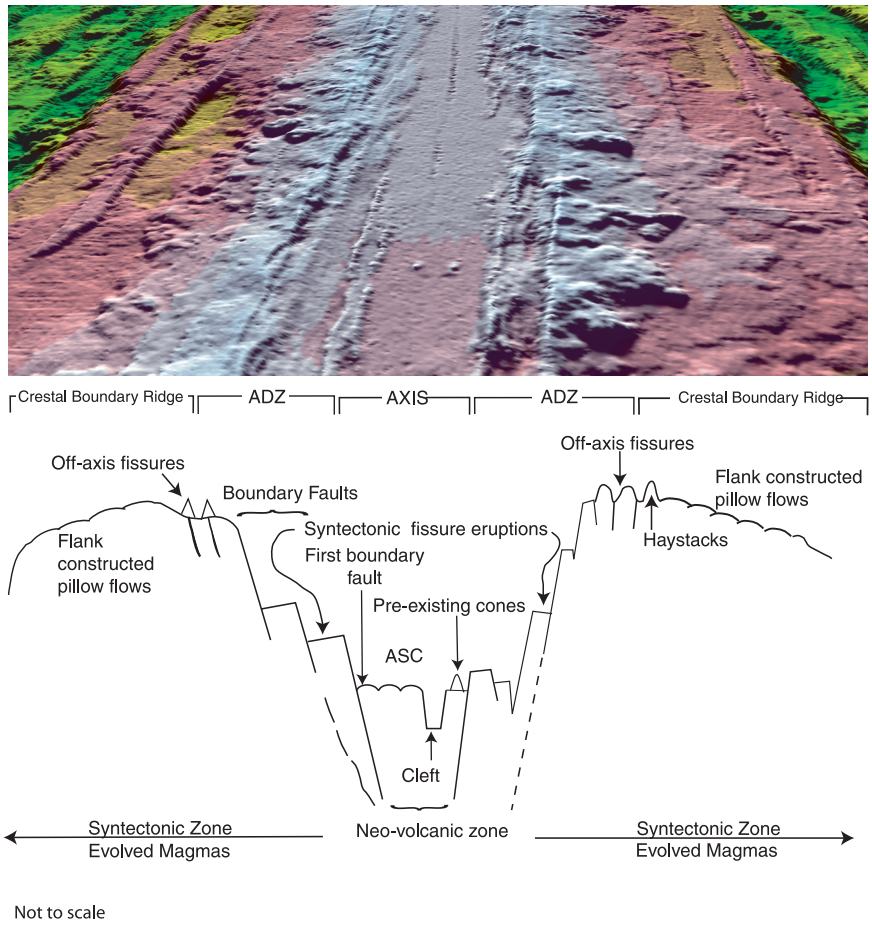

Figure 4. Shaded relief image of the axial bathymetry compared to schematic of volcanic-tectonic regimes of the south Cleft spreading axis (vertical scale exaggerated to illuminate features). The axial valley center is a neovolcanic zone covered by the young sheet flows. The cleft is the axial summit collapse (ASC) trough and the locus of the eruptive fissure for this unit. On either side of the neovolcanic zone is the Axial Disrupted Zone (ADZ). The ADZ on the floor of the axial valley includes broken massive flows with older sulfide spires; open fissures and/or eruptive fissures; and faults that separate intact drained lava lakes. Fissures also typically disrupt the inner face of the CBR, but these are partially covered by syntectonic flows and haystacks. The outer flanks of the CBR are covered with outward flowing pillow and lobate flows with only rare open fissures. The ADZ and the CBR are both interpreted as zones of rapid tectonic extension and syntectonic volcanism.

al., 2006; *Canales et al.*, 2005] that is primarily bounded by constructional ridges with steep, inward-facing, walls (Figure 4). These bounding constructional ridges, referred to as "bowform" ridges by *Kappel and Ryan* [1986] are hereafter referred to as Crestal Boundary Ridges (CBR), to be more consistent with terminology for the EPR. The western boundary of the axial valley is well defined by a continuous inward-facing fault, oriented approximately 020° (Figure 2) while the eastern wall is less clearly defined. The axial valley varies from 1 to 3 km across to the base of the parallel inward facing faults.

[10] There are a series of small faults and associated ridges within the axial valley and adjacent to the CBR bounding faults. These smaller ridges delineate zones of deformation up to 800 meters wide that include smaller step faults, pressure ridges, down-dropped blocks, and exposed slivers of older flows that are partially buried by younger lavas. Here we define this faulted and tectonized zone that includes the terrain between the unfaulted lava-covered floor of the axial valley and the largely unfaulted CBR as the Axial Disrupted Zone (ADZ). It is best imaged in Figures 2 and 4, where the oblique nature of the faults and ridges can be seen.

[11] The CBRs that define the edges of the axial valley are often truncated by inward facing fault scarps. These steep inner walls expose faulted pillowed flows that in some places cap massive flows. Haystacks or flow fronts that dip into the

axial valley are typically truncated by faults or fissures. In contrast, the outer flanks (those facing away from the axis) of the CBRs have very few faults and are composed of extensive areas covered with lightly sedimented lobated and tubular pillows many of which are elongated in the present downslope direction (away from the axis). Conical mounds of tubular and drained-out pillows that resemble subaerial hornitos and the submarine haystacks described on the Mid-Atlantic Ridge [*Ballard and Moore*, 1977, p. 17] are commonly observed in these flow fields. All of the flows that comprise the CBRs are remarkably intact, particularly considering the extent of deformation observed in the "younger" crust within the axial valley. The regional EM300 data are consistent with these observations suggesting that this outer flank topography is constructional, composed of thick, intact pillow flow units with flow fronts tens of meters high and flattened lobate flows up to tens of meters across (Figure 2). Sheet flows and collapsed lobates common in the axial valley are absent as are lava channels commonly found emanating from the ASCT to off-axis areas on the EPR [*Sinton et al.*, 2002; *Soule et al.*, 2005].

[12] On the northern end of the segment, where the northern terminus of the Cleft spreading axis overlaps the Vance spreading axis (Figure 1), the western wall steps westward toward the Vance Segment deepening into a basin. The eastern side of the northern Cleft Segment terminates in small ridges and sprays of pillow mounds that bend westward into the basin and toward the western flank of the Vance Segment. On the southern end of the segment, at the RTI, the axis of the spreading center deepens slightly and curves eastward into and beyond its intersection with the BTZ and is characterized by a series of mounds and curved volcanic ridges that wrap around the nodal basin (Figure 3). These curved ridges appear to be the source vents for a drape of pillowed flows on the walls of the transform corner, cut only by the continuation of along-axis faults. Fresh glassy lavas recovered from these ridges suggest that they include some of the most highly evolved lavas and youngest zones of volcanism along the southern Cleft Segment [*Cotsonika et al.*, 2005].

[13] Along the entire segment, the EM300 reflectivity is uniformly high for both the spreading axis and the adjacent CBR. The flanks beyond the CBR have a lower reflectivity consistent with our observations of significantly increased sediment cover and presumed increased age of the crust.

4. Inferred Age Relationships

[14] Relative ages of the different morphological components were inferred during the ROV dives on the basis of the freshness of the glassy flow margins, amount of sedimentary cover and stratigraphic relationships. Here we designate the youngest to oldest flow units as 0 to 3 respectively, in a similar fashion to the relative ages assigned to EPR lavas [*Haymon et al.*, 1991; *Fornari et al.*, 1998]. For the entire segment, the flows within the center of the axial valley are considered the youngest of all eruptive units or age "zero." The inferred ages progress from the axis to the outer flanks. In North Cleft, the youngest central flow is the "New Pillow Mound" [*Embley and Chadwick*, 1994] that laps against the Lava Rise Ridge and is thought to be contemporaneous with the megaplume in 1986 [*Baker et al.*, 1989]. The Young Sheet Flow in the north is younger than the Lava Rise Ridge but pre-1982 [*Embley and Chadwick*, 1994; *Embley et al.*, 1999]. For South Cleft, the youngest flow is an extensive, chemically homogenous sheet flow that apparently emanates from the "cleft" eruptive fissure (Figure 2, SC-YSF). This "zero age" young sheet flow (SC-YSF) is bounded by slightly older faulted massive flows, which are given a relative age of 1. The walls of the axial valley are highly fissured with massive and pillowed flows that appear older than the flows observed within the axial valley and are given a relative age of 2. Small lava lakes perched on the inner walls of the CBR are considered contemporaneous with these faults (and younger than the crust cut by the faults) and would thus be age 1.5. Pillowed flow fronts within the ADZ flow into the axial valley, but these are typically truncated by faults, as would be expected for syntectonic eruptions. The seafloor exposed completely external to (and partially covered by) the CBR flows are older, and given a relative age of 3. The contacts between the lower older seafloor and the edges of the upper CBR pillowed flows are well defined by both sediment cover and freshness of the glass. Many of the lavas that comprise the CBR have only a moderate coating of sediment and minor accumulations between pillow lobes suggesting they could be as young as age 1 and certainly not as old as the age 3 lavas. The thickness of sediment cover dramatically increases to >1 m at the foot of the CBR covering most of the low-lying flows. Even so, beyond the CBR there

are still faults and fissures that are largely unsedimented and clearly exposed, as well as associated pillow mounds, ridges and haystacks with only light sediment cover protruding above the thick regional sediment cover. The consistent appearance of the unsedimented lava ridges and mounds suggests that these are younger features and not just highstanding and stripped of sediment by bottom currents. Thus although the floor of the axial valley and the inward facing walls represent a consistent age progression, there is not a monotonic increase in age away from the axis. U-series dating of some of the off-axis flows is underway (K. H. Rubin et al., unpublished data, 2005).

[15] A critical geologic and age relationship we have observed is that the lobate and pillowed flows that comprise the outer flanks of the CBR are undeformed, covered with only minor amounts of sediment (some accumulation between pillows), and cover a wide region that is virtually unfaulted, particularly in comparison to the highly deformed "younger" lavas in the ADZ within the axial valley. Wherever we observed these flank lavas on the CBR they appeared to be approximately the same age, regardless of distance from the axis. Given the extensive fissure formation and faulted pillowed haystacks in the ADZ, the undeformed nature of the outer CBR is difficult to explain unless they were erupted on the ridge flanks outside the zone of deformation (ADZ) or escaped deformation during a period of near-axis faulting. Similar relationships have been documented on the flanks of the northern EPR where the crestal plateau is largely covered with undeformed pillowed flows that appear to be approximately the same age [*Perfit and Chadwick*, 1998]. Many of the CBR pillow flows are clearly older than zero age on the basis of the appearance of their glassy crusts and the thickness of Mn-coating on recovered samples, but could be a younger veneer of age 1 or 2 overlying older basement of age 2 or 3. This is consistent with field relationships (i.e., fissure-fed pillow ridges or intact haystacks on top of faulted basement) and the lack of significant sediment accumulation on these units.

5. Regional Structure and Morphology

5.1. Structure of the Cleft Segment

[16] Profiles across the entire section of ocean crust imaged by the EM300 are presented as Transects 1–5 (from south to north; Figure 5) and the bathymetric variations and distribution of faults are plotted in Figure 6. The minimum depth of the CBR varies only slightly from 2200 to 2100 meters along the entire segment and the morphology of the ridges is more symmetrical in the south than in the north. The southern transects show this portion of the ridge is dominated by a 14 km wide axial high plateau bounded by outward facing scarps. The axial valley, boundary CBR and flank graben structures are superimposed upon this broad axial high. The axial high plateau is reminiscent of the axial highs of fast spreading ridges [*Carbotte and Macdonald*, 1994] that are attributed to the buoyancy of the upwelling mantle associated with the spreading center [*Wilson*, 1992]. The 250–300-m high outward-facing scarps are draped with pillowed flows similar in appearance with flows that originated 3–5 km nearer to the spreading axis. Assuming a steady spreading rate of 6 cm/year, these escarpments represent crust that formed approximately 250 kyr ago. The topography beyond these outward-facing escarpments (i.e., in older crust further from the axis) is dominated by the ridge-parallel abyssal hill structure with outward-oriented pillow flow units similar in scale to the CBR.

5.2. Profiles of the Axis

[17] Cross-axis profiles P1, P2, and P3 (Figures 5 and 7) delineate the changing depth and shape of the axial valley with proximity to the Blanco Transform Zone. The most northerly profile near the South Cleft vents (P3 in Figure 7) shows a well-defined central "cleft" within the axis floor, bordered by the subdued steps within the ADZ up to the crestal boundary ridge. Profile P2, crosses the axial valley about 6 km nearer to the RTI than Profile 3, and shows the axial floor is about 10 m deeper with a more weakly defined cleft or ASCT. Profile P1 is only 10 km from the RTI and has an axial floor that is 30–40 m deeper than at P2 and P3 with no cleft present. The faulted ridges that bound the ADZ on the southernmost profile are marked by well defined fault blocks that are steeper and more offset from the inward-facing walls of the adjacent CBR.

5.3. Volumes of Volcanic Features

[18] The volumes of volcanic features (seamounts, lava ponds, aggregate CBR flank, etc) seen on the bathymetric map were calculated using (1) thicknesses derived from the EM300 depths and (2) the areas shown in Figure 5 (Table 1). Measured features were selected to represent typical construc-

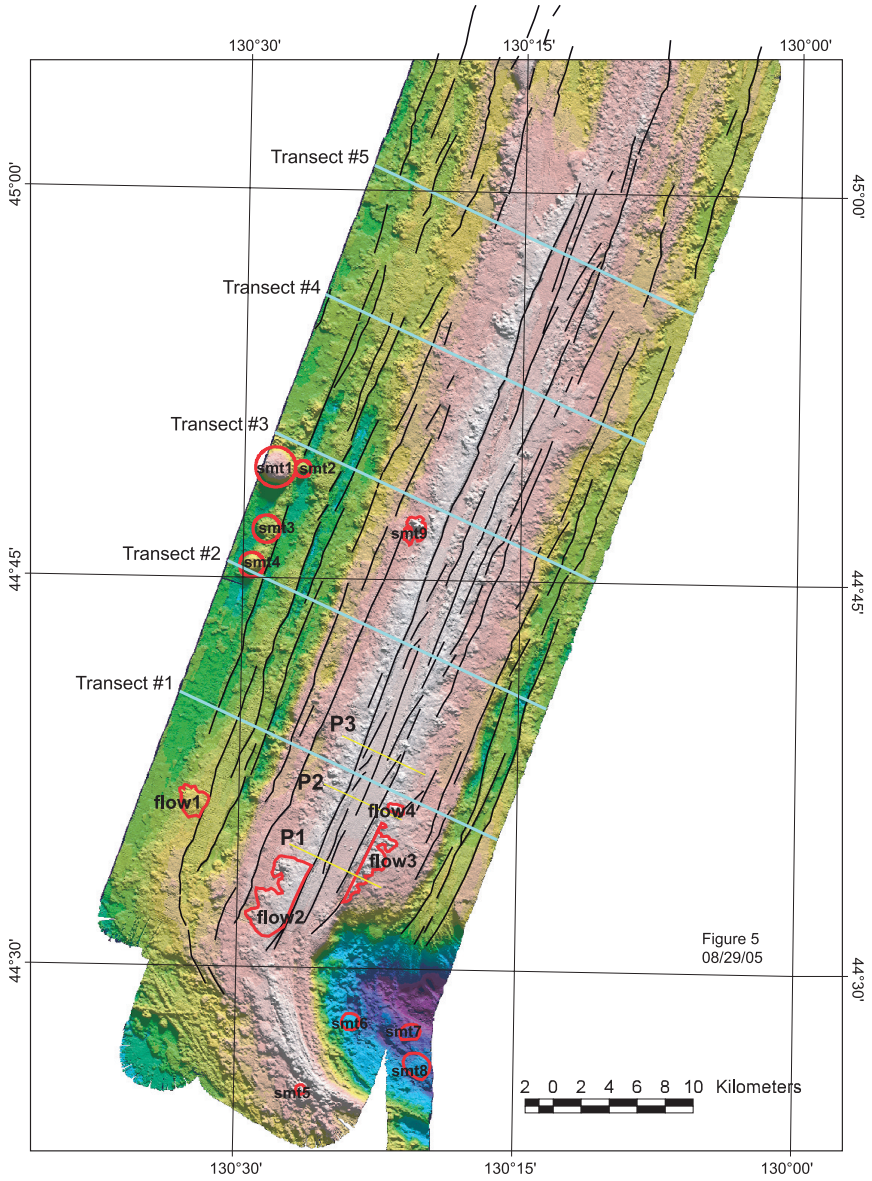

Figure 5. EM300 bathymetric basemap with areas marked for quantitative measurements. Seamounts (SM 1–8) and lava flow units (flow 1–4) were used for volume estimates. Profiles P1-P3 cross the axial valley, and Transects 1–5 are east-west profiles that cross the entire segment.

tional features (volcanic constructs created during one eruptive phase, but likely composed of many individual flows). An ArcView-based tool was used to collect the measurements and calculate the volumes. The baseline of each structure was determined by three measurements on the adjacent seafloor, and the volumes were determined geometrically. The largest near-axis seamount (Figures 5, 8, and 9) has a volume of 1.15 km^3 while the adjacent seamount and the T461 Seamount nearest the axis have volumes that are 0.32 km^3. Smaller mounds have volumes of about 0.1 km^3, comparable to the perched lava ponds or flat-topped cones seen on the south wall of the Blanco Fracture Zone (e.g., smt 5–8, Figures 5 and 3). Such volumes are smaller than most of the historical flows identified on the JdFR and Gorda ridges (7.8–55 km^3 [see *Chadwick et al.*, 1998; *Perfit and Chadwick*, 1998]), but are comparable to the estimated eruption volume per 1000 a. for the Vance seamount chain [*Clague et al.*, 2000] and the annual volume of magma required to sustain the subcaldera magma chamber at Kilauea [*Denlinger*, 1997]. The calculated volumes of the most prominent CBR upper pillow units as delineated in Figure 5 vary from 0.7 to 0.05 km^3; about

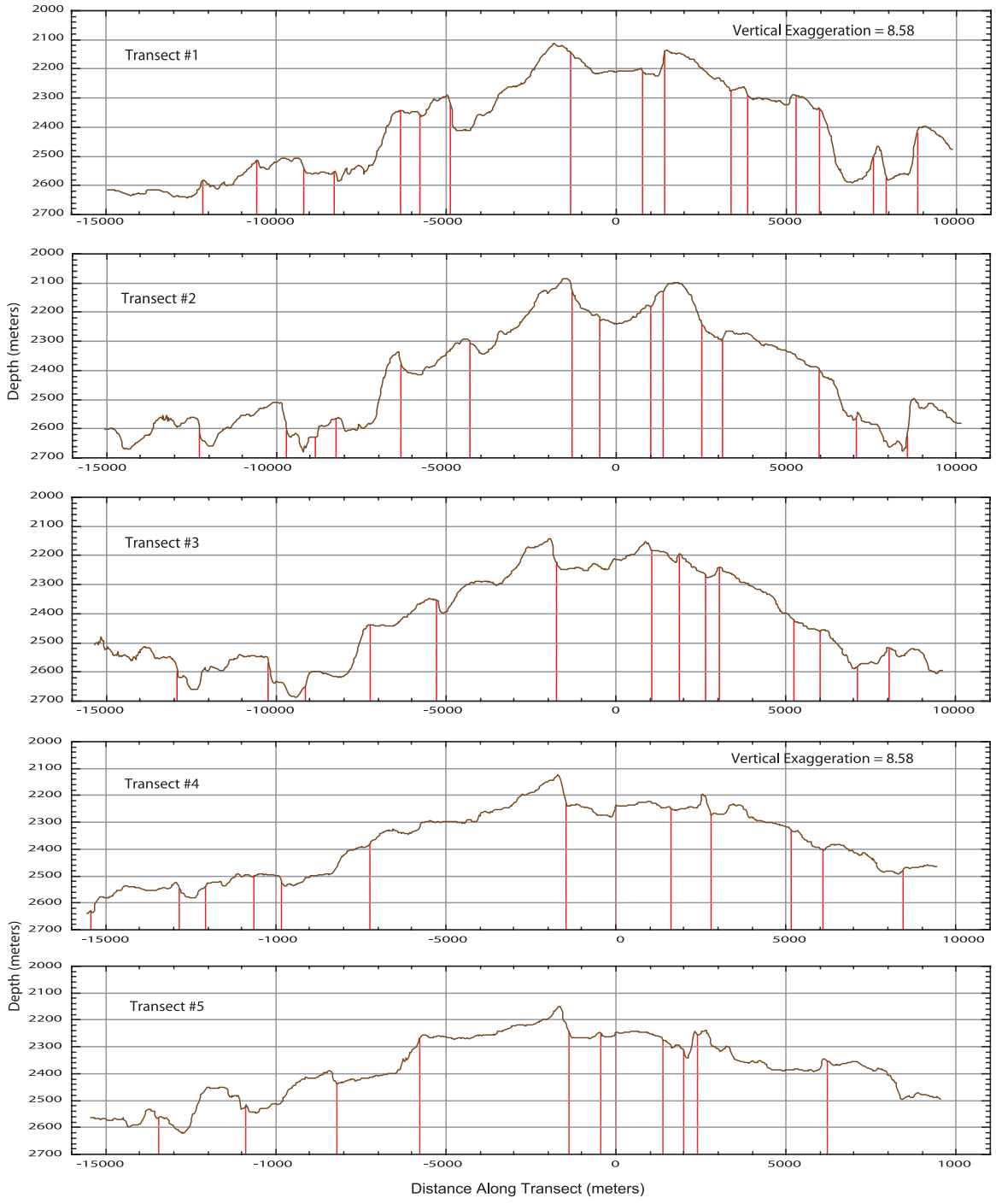

Figure 6. Series of five bathymetric profiles from south to north identified as transects 1–5 in Figure 5. Red vertical bars show the locations of the intersected fault segments from Figure 5. The vertical lines are locations, not fault orientations. The distribution of the faults is compiled as Figure 10. Note the width of the axial high compared to the CBR and axial valley.

half the volume of the seamounts (Figures 9 and 10) and spread over a larger area. Such volumes are more comparable to estimates of flow sizes on the Northern East Pacific Rise [*Perfit and Chadwick*, 1998; *Rubin et al.*, 2001]. Taking the western boundary ridge (flow 2 in Figure 5) as a maximum size of volcanic construction on the ridge flank, simple calculations suggest that the accumulated flows that comprise the CBRs could be as much as 150–250 meters thick within 2–3 kilometer of the spreading axis in this environment This assumes that the baseline is the outer, older seafloor and that

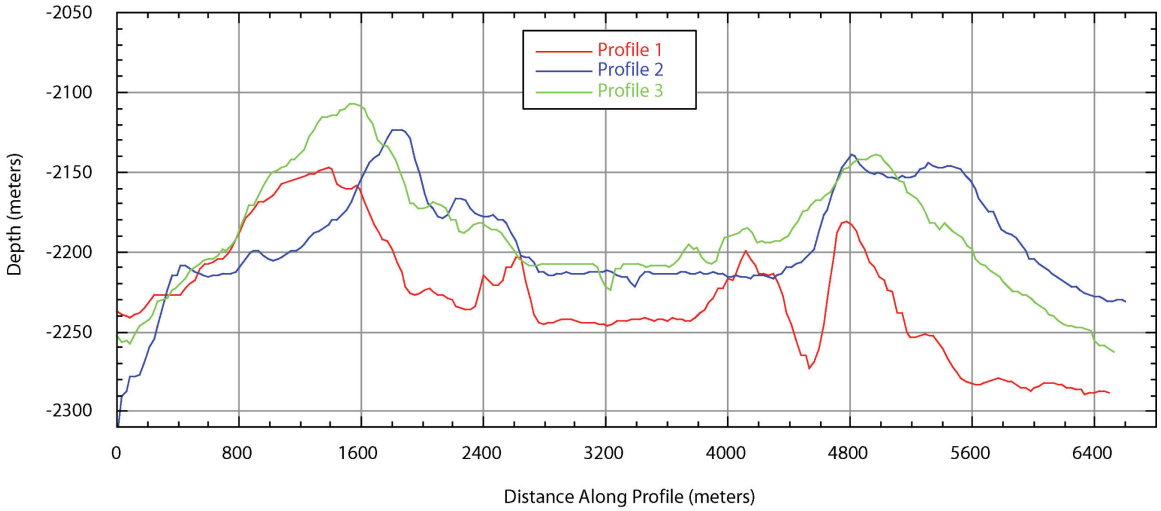

Figure 7. Three bathymetric cross sections across the axial valley and crestal boundary ridges based on the EM300 data as indicated in Figure 5 as P1-P3. Note the increasing depth of the axial valley floor, and disappearance of the "cleft" eruptive fissure and the more well-defined appearance of the ADZ faulted ridges with proximity to the RTI.

much of the CBR topography is volcanic eruptions versus uplift. This latter assumption is supported by the observation of significant syntectonic flows infilling and/or covering the ridge-parallel faults and fissures.

5.4. Fault Orientations and Relationship to Spreading Regime

[19] Inferred fault traces based on strong structural lineations in the bathymetry (Figure 5) have a varying orientation along their length. In many cases the presence and orientation of the faults was confirmed during ROV traverses. The variable orientations were quantified by dividing each fault segment into 3 km bins and then measuring the exact orientation of each bin (Table 2; Figure 10). Faults and fissures along the Cleft Segment, including the "cleft" itself, have an azimuth of 025°, which suggests a local volcanic spreading direction of 295°. Ridge-parallel faults are present on both sides of the axial valley and extend for the entire segment (up to ~58 km long). Individual ridge-parallel faults up to 30 km long can be traced on the flanks. Near 44°45′N, faults step to the NW in en echelon fashion on the west side of the axis in smaller 4–10 km segments. The en echelon segments vary from ridge parallel (026°) to slightly oblique (031°). Some of the longer, ridge-parallel structures are offset by shorter segments, which are oblique to the spreading axis (037°). Strongly oblique ridges within the axial valley (046°–047°) (Figures 2 and 5) and oblique fractures connecting en echelon fault segments (049°) (Figure 8) are orthogonal to the direction of absolute plate motion (313°; NUVEL-1A [*Gripp and Gordon*, 1990]) rather than the local spreading direction.

[20] The fault distribution (Figure 10) is asymmetric with more numerous near-axis faults on the eastern ridge flank compared to the western flank with fewer faults on the eastern flank overall that are further from the spreading axis compared to the western side. On the west side of the spreading axis, about 10 km off-axis from the segment center,

Table 1. Estimated Volumes of Constructional Volcanic Features (Figure 5)[a]

Feature ID (Figure 17)	Volume, km^3
smt1	1.150
smt4	0.320
smt3	0.320
smt2	0.100
smt9	0.090
flow4	0.050
flow3	0.710
flow1	0.140
flow2	0.690
smt8	0.140
smt7	0.090
smt6	0.090
smt5	0.020

[a] The thickness is the difference in elevation of surrounding seafloor (based on the average of at least three measurement points) and height of the volcanic feature, with a correction for the local slope of the seafloor. Calculations do not consider underlying topography or any subsidence due to the loading of the volcanic pile.

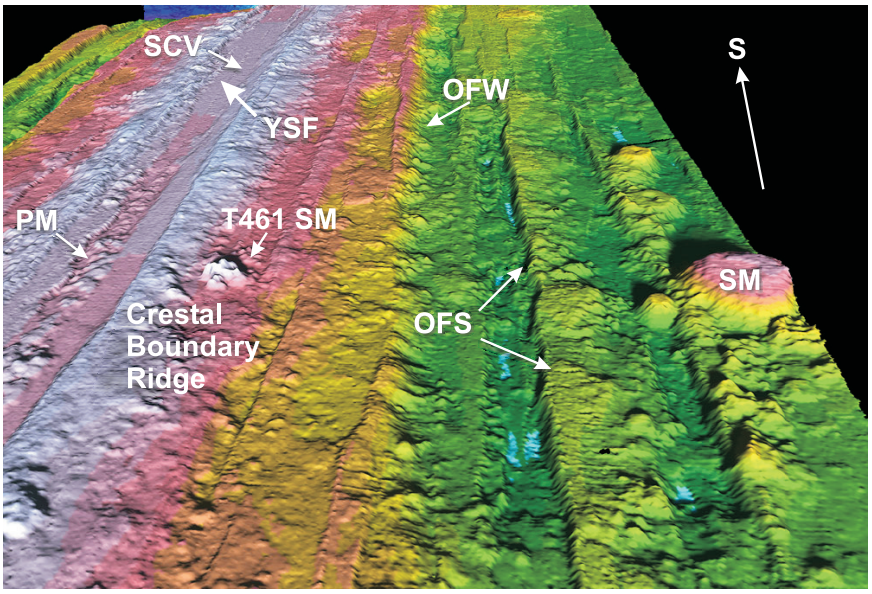

Figure 8. Shaded relief image of the Cleft center and west flank seamounts from the north looking to the south. OFS, oblique fault segments associated with regional plate motion stress field. PM, pillow mounds that fill the axial valley at the center segment discontinuity. SCV, the south cleft vents visible to the south. SM is a near-ridge seamount perched on the edge of an abyssal hill fault. T461SM is the small seamount visited on dive T461. Neither seamount appears related to the ridge magmatic system. OFW is the first major outward facing fault on the west side of the spreading axis. YSF, the young sheet flows present in the south Cleft vent area.

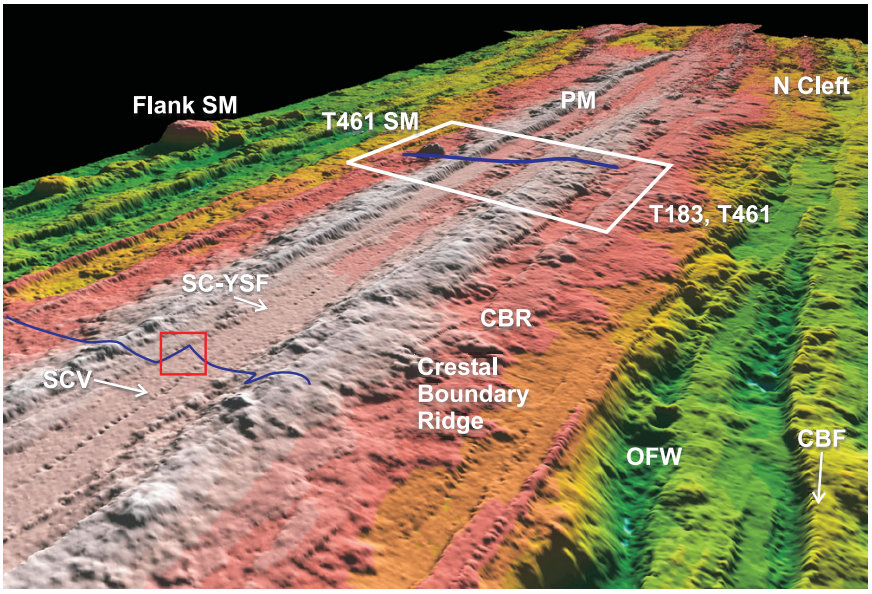

Figure 9. Shaded relief image of the south Cleft axis and eastern flank from the southeast looking northwest. The southern eastern flank is cut by ridge parallel grabens and curved faults (CBF) reminiscent of propagating rifts. The tilted walls bounding the axial valley and the eruptive edifices that cover them are distinct in this image. OFW, the outward facing wall on the east side of the spreading center; SCV, the south Cleft vents; PM, the pillow mounds as in Figure 8. Large white box shows the area of Figure 15. Dive track for T183/T461 is blue line in box. Dive track for T180/T181/T459 is blue line to south with red box showing location of foundered massive flow shown in Figures 17a and 17b.

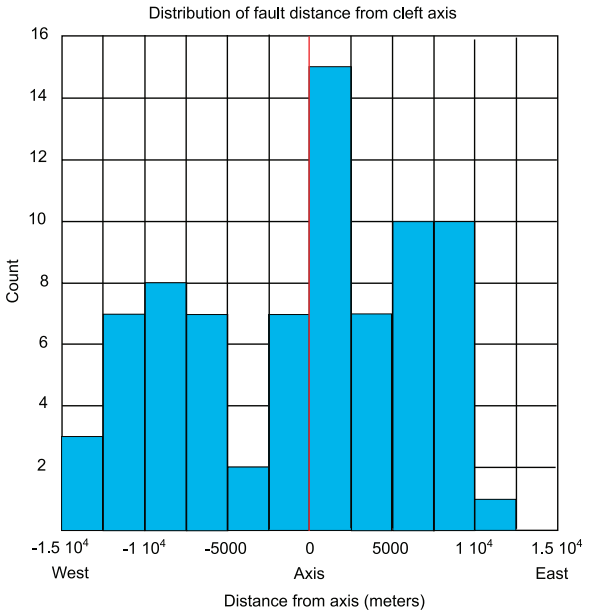

Figure 10. Histogram of fault distribution from transects shown in Figure 5. Note that the eastern side of the ADZ has a larger number of faults.

axis-parallel faults are broken into a series of small en echelon segments oriented oblique to the ridge axis (Figure 8). These segments are oriented approximately 030° compared to the axis-parallel structures that are 025°. The oblique fault segments (OFS in Figure 8) are most conspicuous within the central region where there appears to be ridge-flank seamount formation.

6. Magnetic Transects

[21] The ROV dive transects completed in 2000 and 2002 allow us to construct five composite near-bottom magnetic profiles across the Cleft spreading axis from central cleft to the southern terminus of the segment. The raw magnetic data were collected with a 3-axis sensor, which required calibration and correction for the permanent and induced magnetic effects of the ROV. We vector-summed the three field components to calculate total field as no independent sensors were available for pitch and roll measurements. Sensor calibration was carried out by performing a compass-spin maneuver at a mid-water depth during descent and ascent of the ROV. The magnetic effects of the vehicle, which typically were in the range of 3000 nT were reduced to less than 100 nT after calibration. After combining the magnetic data with the depth and navigation data, we removed the regional field based on the International Geomagnetic Reference Field (IGRF) model for 2000 and 2002 [*International Association of Geomagnetism and Aeronomy, Division V, Working Group 8*, 2000]. Individual ROV dives were then combined into composite profiles (Figure 11). Although no altimeter data were available, the depth of the ROV is known as is the bathymetry from the EM300 data. The ROV depth data was checked against bathymetry profiles extracted from the EM300 data to ensure that navigation and depth ranges were coincident. The magnetic effects due to the undulating depth of the ROV require upward continuation of the magnetic field data to compensate for these effects and for inversion to crustal magnetization. We used the *Guspi* [1987] method to continue the magnetic field data to a level plane above the topography. The resultant profiles are shown in Figure 11. The *Parker and Huestis* [1974] Fourier transform method was used for inversion of the upward continued data to crustal magnetization. This approach removes the effect of topography from the signal but assumes (1) a constant magnetic vector direction, which we assume is in the direction of the present field, and (2) a constant thickness source layer. For these calculations we assumed a 500 m thick source layer, which is compatible with the average thickness of the extrusive layer at the Cleft Segment based on seismic data [*Canales et al.*, 2005].

[22] The upward continued magnetic anomaly profiles (Figure 11) show a strong 2500 nT magnetic peak located over the axial valley and generally centered over the "cleft." This central anomaly peak decreases toward both east and west boundary walls of the axial valley with magnetic anomaly lows located at the base of these valley walls. The ADZ and older sheet flows (OSF mapped on dive T183) located at the boundary walls appear to have distinctly separate magnetic field anomalies associated with them. In general, the CBR also have associated magnetic anomaly highs. Additional

Table 2. Orientation of Structural Features (From Figure 5)[a]

BIN	Orientation	Location	Orthogonal
1	025–026	ridge parallel	295–296
2	035–037	en echelon off-axis	307
3	046–047	axial valley oblique ridge	314
5	049	oblique short	319
6	031	en echelon off-axis	301
		N. Cleft LPM	310
		Vance chain	324
		absolute plate motion	313

[a] Notes: All fissures and faults apparent on EM300 data were divided into 3 km segments. The orientation of each segment was determined and placed into one of 6 bins.

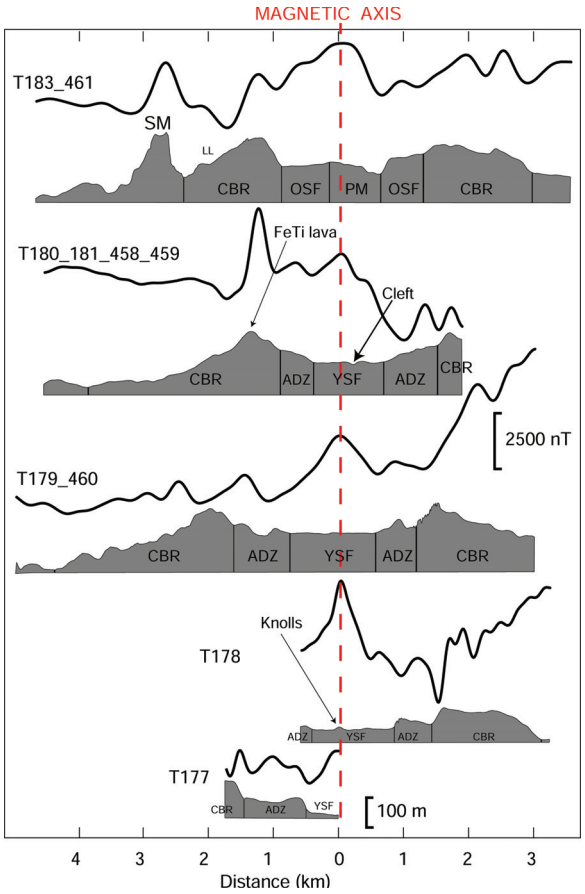

Figure 11. Composite upward continued (2.1 km level) near-bottom magnetic field profiles (bold lines) collected during ROV dives across the spreading axis of the central to south Cleft region from north (top) to south (bottom), respectively. ROV dive numbers are identified. Shaded profiles are the depth of seafloor obtained from the ROV. Profiles have been centered on the axial magnetic anomaly high, which also aligns with the center of the axial valley. Depth profiles have been divided into the various geologic zones as discussed in the text with the following abbreviations: CBR, crestal boundary ridge; OSF, older sheet flow; PM, pillow mounds; YSF, young sheet flow; ADZ, axial disrupted zone; SM, seamount; LL, lava lake on dive traverses T183–T461. FeTi refers to highly evolved iron- and titanium-rich lavas found at that location that correspond to a strong magnetic anomaly.

discrete anomalies are found on each profile. For example, Profile 183_461 shows a magnetic peak associated with the small off-axis seamount to the west. Presumably this is due to the extra volume of magnetic material of the seamount and/or the youthfulness of the volcanic units. Profile T180_181_458_459 shows a strong local magnetic anomaly over the western CBR. This appears to correspond to an area floored by ferrobasalts and ferroandesites that were sampled at this locality. The eastern CBR flanks appear to be quite magnetic on profiles T179_460 and T178. These observations are confirmed in the magnetization inversions shown in Figure 12 that remove the effect of topography from the signal. For the inversions, the maximum magnetization (10–20 A/m) is located over the axial valley symmetry center, the "cleft," and the young-looking sheet and lobate flows that cover much of the floor of the axial valley. This central magnetization high appears to be approximately 1 km wide but narrower to the south (e.g., 500 m wide on profile T178, Figure 12). The edges of the axial valley are

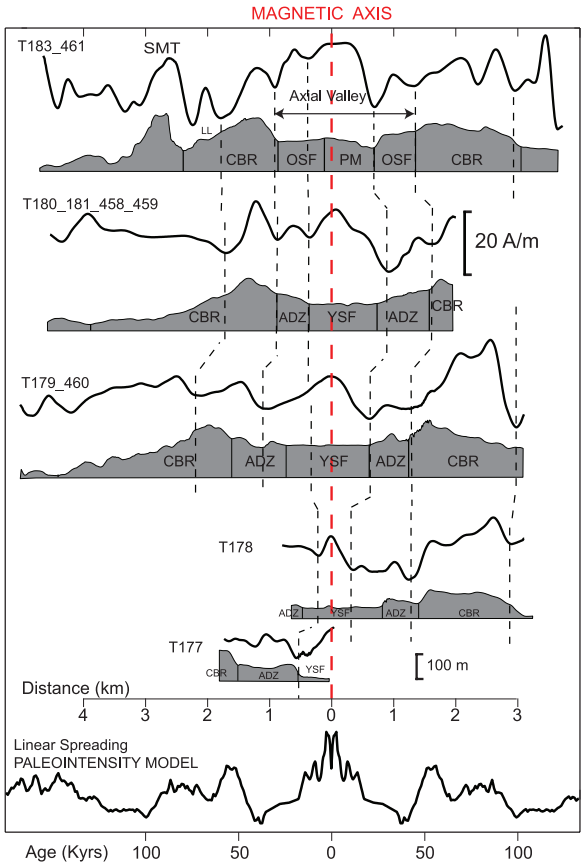

Figure 12. Composite magnetization inversions of cross-axis near-bottom magnetic field profiles. Bold lines are the magnetization inversions assuming a constant 500 m thick source layer whose upper bound is the seafloor topography shown shaded. Bold (red) dashed line marks the axis of the magnetization high and the apparent line of symmetry; the thinner (black) dashed lines indicate the correlation between profiles. The bottom profile is a forward model of paleointensity variations based on *Guyodo and Valet* [1999] and archeomagnetic data [*McElhinny and Senanayake*, 1982] and shows a remarkable similarity with the magnetization results both on axis and with the flanking CBR regions. Abbreviations as defined in Figure 11.

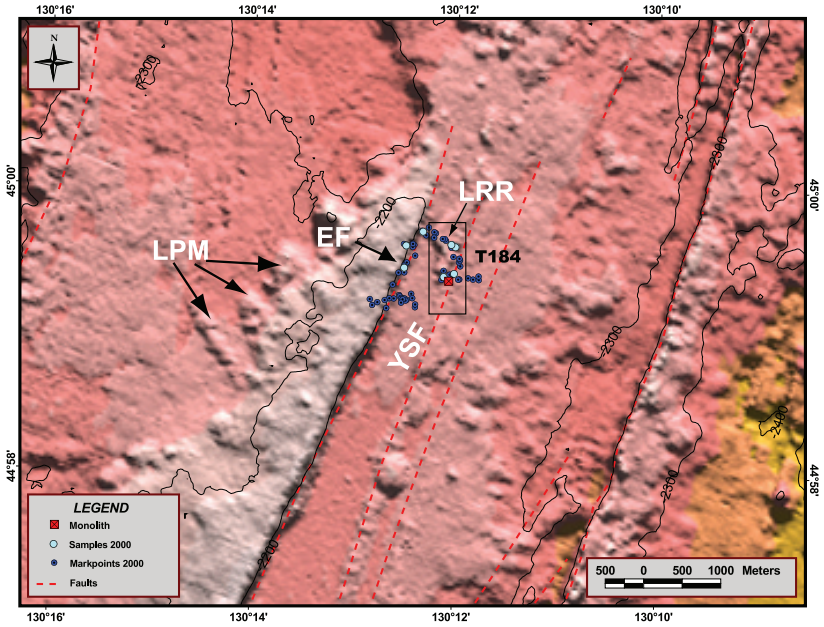

Figure 13. ROV dive map for T184 with annotations. Note that the dive track, sample locations, and markpoint observations are logged in real-time using ArcNav, an ArcView-based navigation and archival system used for all the dives in this study. Positions and observations (including framegrabs) of markpoints are available as auxiliary material. Box shows area of Mesotek high-resolution acoustic survey described by *Chadwick et al.* [2001]. LRR, lava rise ridge; YSF, North Cleft young sheet flow; LPM, linear pillow mound. An eruptive fissure (Figure 14a) is located at the base of the western CBR and within the ADZ. The location of the Monolith vent site is shown as a red square. Red dashed lines indicate fault traces.

uniformly marked by low magnetization. The ADZ appear to have intermediate magnetization values while the flanking CBR appear to be as strongly magnetized as the axis, especially on the eastern side for profiles T179_460 and T178.

7. ROV Dive Observations

[23] The integration of the bathymetric data with observational and sample data obtained during the ROV dives provides an opportunity to identify specific outcrop relationships to corroborate regional relationships. For the purposes of discussing the geology, we have divided the Cleft latitudinally into four areas: North Cleft, Central Cleft, southern Cleft Vent area, and the Southern Terminus. Within each of these areas, we compare the nature of the spreading axis, the transition to the bounding faults and the off-axis flanks. Thus our data constrain both the along-ridge and cross-ridge geological and petrological variations of the segment.

7.1. Northern Cleft (Dive T184)

[24] The axial portions of north Cleft (Figure 13) have been visited during numerous previous expeditions, as this is the site for which an eruption and associated "megaplume" were first identified [e.g., *Embley et al.*, 1991; *Chadwick et al.*, 1991; *Baker*, 1994; *Baker et al.*, 1989]. Previous submersible and geochemical studies of North Cleft suggest the chemically homogeneous "young sheet flow" (YSF) that covers much of the western axial valley may only be a few decades old and is likely related to the active hydrothermal systems in this area [*Embley et al.*, 1991; *Smith et al.*, 1994]. The older "lava rise ridge" (LRR) [*Chadwick et al.*, 2001; *Embley and Chadwick*, 1994] and the YSF immediately to the south of it are clearly recognizable in the bathymetric images (Figure 13). Our single ROV dive T184 crossed these units or their equivalents as well as visiting the Monolith vent. In 2000, Monolith had coalesced into a still-active edifice with three spires all perched on the edge of a fractured massive flow unit.

[25] The western boundary wall of north Cleft exposes truncated pillow forms and elongate pillows on top of thick sheet flows (unrelated to the YSF) that are cut by extensive fissures generally less than a few meters wide. At least two of these ridge-parallel fissures, on top of the western CBR, were partially filled with pillow basalts that were younger than the surrounding flows. The southern

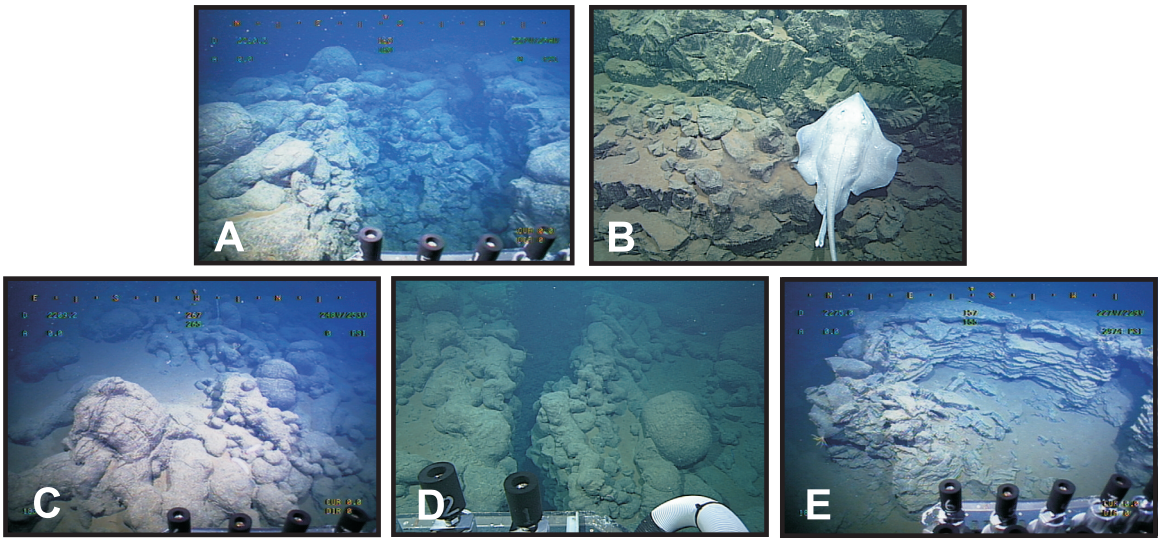

Figure 14. Selected framegrabs taken from the ROV Tiburon from dives T184 (north Cleft) and T183/T461 (central Cleft): (a) Eruptive fissure observed within the western ADZ of the north Cleft segment. (b) Massive flows on the western sides of the axial valley (with ray for scale). (c). The eastern crestal boundary ridge (CBR) with cascades of lobate flows dipping to east. (d) Fissures decorated with younger pillows on the eastern CBR. (e) Intact collapse structure observed on the floor of the graben on the eastern flank of the CBR, 3.5 km from the spreading axis.

extension of one of these fissures, at the base of the western boundary wall, was completely filled with pillow lava (EF in Figure 13) that extruded from this feature (framegrab, Figure 14a). Similar relationships are present at many other off-axis locations and we interpret them as off-axis eruptive fissures. They are similar in size and form to the recent eruptive sites along Axial Seamount and the EPR at ~9°55′N [*Perfit and Chadwick*, 1998]. On the western edge of the CBR, a series of small linear pillow mounds emanate from the western axial ridge at an azimuth that trends semi-parallel to the general seamount trend of 324°–331° (Figure 13) [*Clague et al.*, 2000].

7.2. Central Cleft (Dives T183, T461)

[26] The smooth morphology of the young sheet flows characteristic of north Cleft and the south Cleft vent areas gives way to relatively young-looking pillowed volcanic mounds that fill the center of the axial valley (at 44°47′N) in the central Cleft region (PM in Figures 8, 9, and 15). The axial pillow mounds are bounded by older sheet flows (OSF) on the basis of the paucity of fresh glass and sediment cover in the latter terrain. In contrast, the pillowed flows in this area are considered younger, with very fresh glass, albeit covered with hydrothermal precipitate. The pillows cover fissured massive flows (Figure 14b) and appear to pour into a large fissure at the eastern contact between the old sheet flow (OSF) and the pillow mounds (PM).

[27] The eastern and western CBR in the central Cleft area are not perfect mirror images of each other. As can be seen in Figures 8, 9, and 15 (and verified by visual observations and magnetic data), the western CBR is structurally well-defined, continuous with north and south Cleft and is marked by a distinct inward facing boundary fault. Similar to N. Cleft, the western CBR also has open, meter-wide fissures at the base of the wall, fissures near the summit, and a continuous and unfaulted drape of pillowed flows that covers the outer western flanks of the CBR (Figure 14c). Lava channels composed of sheet and lobate flows that commonly extend from the axis to off-axis areas of the northern EPR [e.g., *Fornari et al.*, 2004; *Soule et al.*, 2005] are noticeably absent from the CBR. Relict volcanic haystacks and small piles of pillows perched on the edges of fissures adjacent to the flows suggest local eruptive fissures (Figure 14d). Haystacks observed within or adjacent to the ADZ have flow fronts that drape into the axis, typically truncated by the faults within the ADZ. In addition, during the T461 transect, a perched lava lake (visually identified by drainback features; see LL in Figure 15) was observed near the summit of the western CBR delineated by local eruptive fissures. The 170 meter-high volcanic construct traversed during T461 (SM in Figure 15) is a small, young-

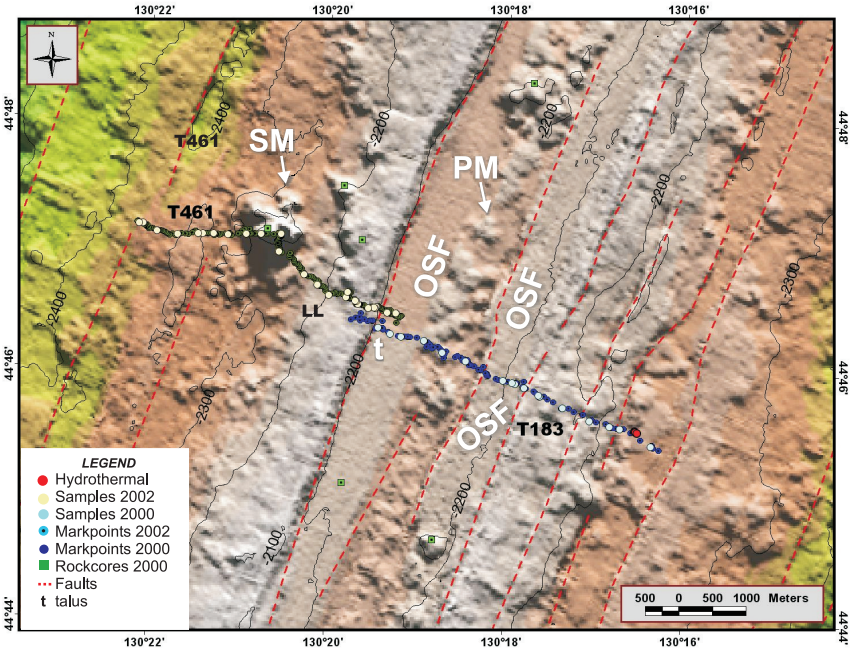

Figure 15. ROV dive map for T183 and T461 with annotations. Dots represent mark points along dive traverse with open symbols representing sample locations. Green squares are positions of glass rock cores. Low-temperature vents discovered on east flank were characterized by thick cover of microbial mat with amorphous precipitates rich in Fe and Si and less Mn [*Stakes et al.*, 2003a, 2003b; D. Stakes et al., manuscript in preparation, 2006]. OSF, older sheet flows; PM, younger pillow mounds. T461 SM is same as previous figures, a young-looking, near-axis seamount with chemistry distinct from axial flows.

looking seamount that does not appear to be magmatically related to the Cleft lavas. The edifice has lavas with distinctly higher MgO contents (~10 wt.%) and more depleted incompatible trace element contents (M. R. Perfit et al., manuscript in preparation, 2006). Rather, it appears to be related to off-axis volcanism with sources similar to the Vance Seamounts to the north. It is composed of very glassy plagioclase-phyric basalts with delicate pillowed forms and elongate tubes. The seamount is superimposed upon the flank topography of pillow flows and haystacks perched on the edges of ridge-parallel fissures.

[28] The eastern CBR was crossed and extensively sampled during dive T183 (Figures 9 and 15). This eastern flank is more faulted than the western flank, with a subdued horst and graben morphology superimposed on the flank. The topography can best be observed on the eastern end of the T183 dive track where a graben 3.5 km east of the spreading axis is floored by a relatively unsedimented sheet flow (Figure 14e) near a low temperature active vent (see auxiliary data for framegrab). Although lobated and pillowed flow morphologies dominate this area, several haystacks (conical mounds in Figure 15) are perched on the corners of faulted blocks. Tectonically disrupted blocks of seafloor are draped with steeply dipping flow fronts and topped with haystacks characterized by symmetrical flows oriented downslope on both east and west sides (Figure 14c). The volcanic edifices observed during this dive partially drape faults or fissures and appear to be contemporaneous with fault formation similar to that described for the EPR (e.g., syntectonic volcanism [*Macdonald et al.*, 1996; *Macdonald*, 1998]). The haystacks and pillow mounds are petrologically similar to the other basalts on the CBR and are not petrologically or morphologically similar to the T461 seamount or presumably the larger, better-defined seamounts to the west (Figure 9).

7.3. Southern Section Near South Cleft Vents (Dives T180, T181, T458, T459, T736)

[29] The ROV crossed the axial valley near the south Cleft Vent 1 site during dives T180 and T458 (Figure 16). The flank to the west of the vents was explored during dive T181 and the eastern flank was mapped during dives T459 and T736. The central portion of the axial valley is characterized by the well-defined ASCT or "cleft" discussed

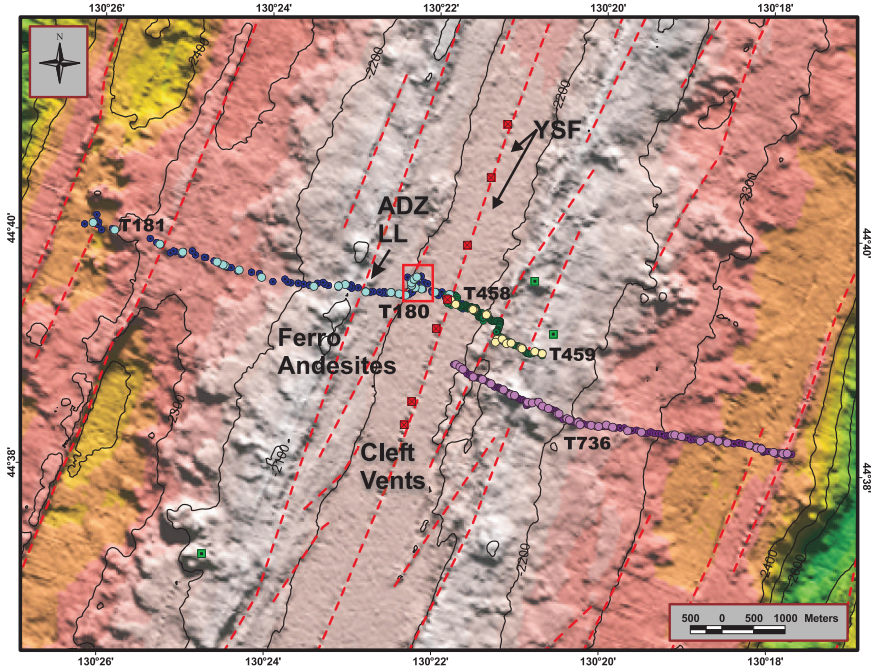

Figure 16. ROV dive map for T458/T459, T180/T181 and T736. Red squares are the South Cleft high-temperature vent sites. Large red box is location of broken massive flow shown in Figures 17a and 17b. YSF, south Cleft young sheet flows; ADZ, axial disrupted zone. LL shows location of perched lava lake that looks like an EPR ASCT except that it is within the ADZ. Location of ferroandesites on western CBR is also shown. Other symbols as in Figure 15.

above that hosts a series of active high-temperature vents (Figures 2, 9, and 16) [*Normark et al.*, 1987].

[30] The axial valley depth is shallower around the South Cleft Vents (SCV) and covered by a smooth, continuous floor of lobate and sheet flows (referred to here as the south Cleft Young Sheet Flow (SC YSF)) with numerous shallow drainback and collapse features (Figures 9 and 16) that increase in abundance toward the cleft. This most-youthful volcanic unit is centered on the cleft and clearly erupted from the cleft eruptive fissure. The SC YSF has been described in detail by *Normark et al.* [1987] and *Chadwick and Embley* [1994], and the chemically homogeneous sheet/lobate flow unit has been taken to represent the composition of the most recent South Cleft lavas [*Smith*, 1993]. Although similar in appearance and likely close in age to the North Cleft YSF, it has a distinctly more evolved composition [*Smith et al.*, 1994].

[31] On the west side of the axial valley at the base of the west wall, there is a disrupted platform of massive flows crosscut by faults that are oblique to the axial structural trend (Figures 9, 16, and 17). The edge of this platform was examined in detail during dives T180 and T181 (Figure 16) and consists of thick units of a broken and foundered massive flow in contact with and in some places partially covered by a younger lobate flow (Figure 17, framegrabs a and b). Some of the blocks are up to a few meters thick, dip toward the axis and enveloped in the younger flow unit (Figure 17, framegrabs a and b). Numerous inactive 1–4 meter tall sulfide spires are perched on the top surfaces of the blocks of massive flows. The presence of these largely intact chimney structures suggests there was a relatively recent period of intense hydrothermal activity unrelated to the "cleft" activity. Visual observations reveal that the contacts between the younger lobate flows and massive blocks are very sharp and unfaulted giving the blocks the appearance of "floating" in the lobate flows (Figure 17, framegrabs a and b). The massive flow blocks appear to have dropped down and inward prior to the eruption of the lobates, perhaps associated with the formation of the ridge-oblique faults in the ADZ.

[32] West of the faulted massive flow, between the edge of the massive platform and the sharp fault scarp that defines the next inward facing fault zone, there are remnants of a lava lake perched on a bench between faults (see Figure 9, LL in Figure 16). Although located between major faults in the ADZ, this lava lake structure shows little

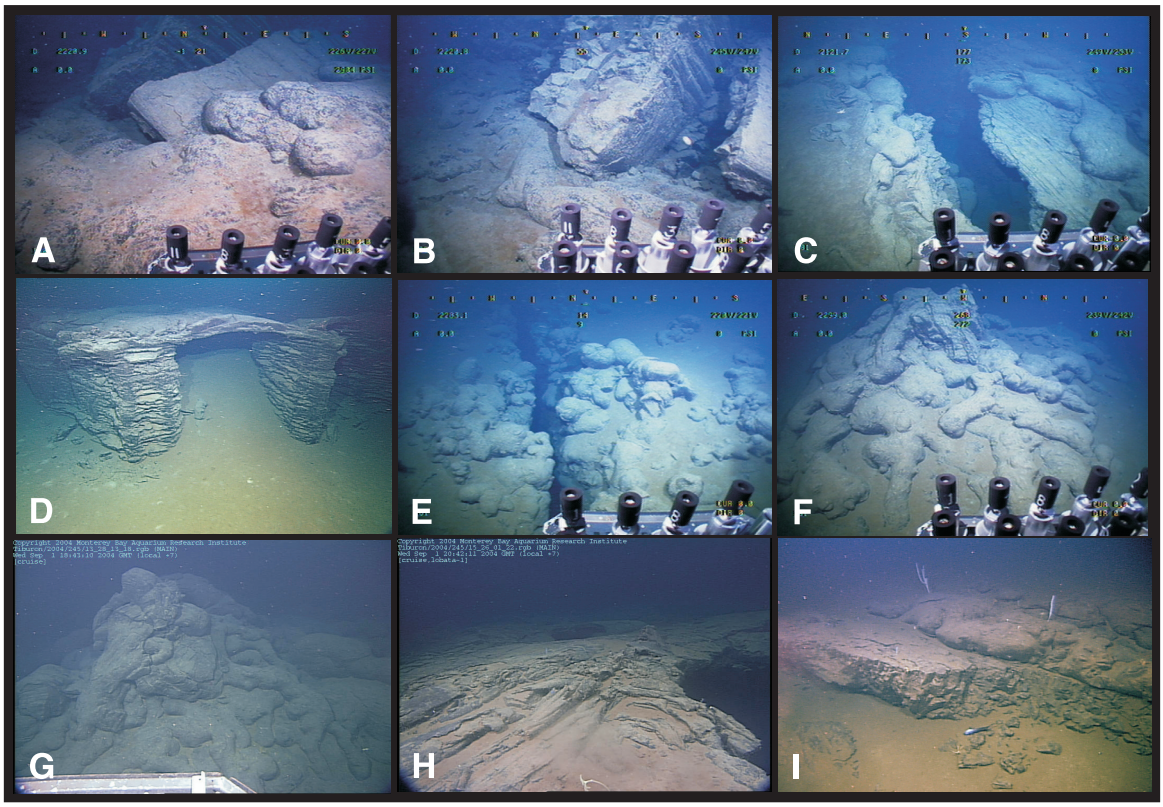

Figure 17. Framegrabs from ROV dives T180/T181/T736. (a and b) Dismembered and tilted massive flow completed surrounded by younger lobate flows in the axial valley; (c) summit of CBR with fissured terrain, location of sample T181-G8; (d) drainback feature located over 4 km west of spreading axis at ridge-parallel fault and east of (e) eruptive fissure on western boundary ridge to east of Figures 17d and 17f; (f) haystack on western crestal boundary ridge to west of Figure 17e and east of Figure 17d; (g) haystack 2.3 km east of spreading axis (same location as sample T736-G16); (h) collapse that is 3 km east of spreading axis (same location as sample T736-G27); and (i) bottom of east flank graben 4.5 km off-axis (same location as sample T736-G36). All sample locations provided in the auxiliary material.

disruption of sheet and lobate flows that comprise it and includes lava pillars, and drainback and collapse features. The delicate collapse structures and upright pillars together with the absence of faults suggest that this eruptive unit was erupted locally, and was *not* tectonized during formation of the ADZ nor transported outward from the axial volcanic zone. The geochemistry (iron-rich basalts and andesites) of the samples from this area and their apparent high magnetization (see previous section and Figure 12) also points to an off-axis or ADZ origin; they are significantly more evolved than those that characterize the homogeneous zero-age flows in the axis (M. R. Perfit et al., manuscript in preparation, 2006).

[33] Structures on the CBR and the flanks were observed in detail on dives T181 (west flank) and T736 (east flank). Dive T736 covered over 5 km off axis on the eastern flank (Figures 1, 9, and 10) and included sections with the most voluminous pillowed flows on the CBR. The eastern ADZ is clearly shown in Figure 2 and includes open, ridge-parallel fissures with haystacks constructed on the intervening crust (e.g., Figure 17g framegrab, 2.3 km off axis). At a distance of 3–5 kilometers from the axis, lightly sedimented sheet flows with lava pillars (Figure 17h framegrab, 3 km off axis) are present. At 4–5 kilometers off axis, a well-defined graben (Figure 2) exists on the edge of the ridge flank, just west of the conspicuous eastward-facing escarpment. This graben is 1 km across and 85 meters deep, and is floored by an only lightly sedimented sheet and lobate flows (Figure 17i framegrab), not consistent with its age assuming it was formed by eruption in the axial valley.

[34] The western flanks of the CBR explored during dive T181 exposed less outcrop with much less tectonism: open fissures on the innermost (easternmost) shoulder give way to unfissured outward flanks completely covered with elongate

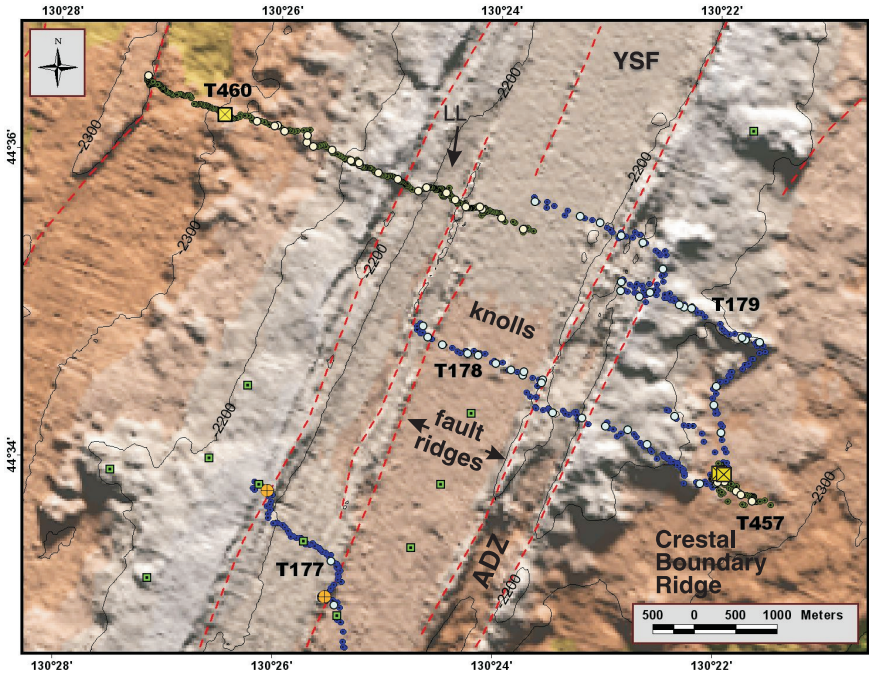

Figure 18. ROV dive map for T177, T178, T179, T457, and T460 with annotations. Note location of low-temperature vents observed on eastern side and western sides of the CBR (yellow boxes). LL is the location of the drained, but intact lava lake shown in Figure 19g. Knolls observed in center of axial valley are older pillowed flows that have fractionated compositions partially overlapped by massive south Cleft young sheet flows (YSF). The linear eruptive edifice examined in detail during Dive T179 was found to be a series of fissure or fault bounded haystacks rather than a single coherent pillowed flow unit. Yellow circles with crosses on T177 are locations of drillcores taken by ROV from large andesite pillows (see image in the auxiliary material). Small green squares are locations of rock core glass samples.

pillowed flows oriented downhill to the west. As in the north, lava channels of sheet flows are absent. Ramparts of pillow lavas and small haystacks concentrated along the edges of the open fissures suggested to us that these are artifacts of lavas erupted from the (1–3 m wide) fissures, perhaps burying older tectonized terrain (see Figures 17c, 17e, and 17f). Beyond the toe of the western CBR flank the seafloor is sedimented except for prominent linear pillow mounds that crop out of the sediment every few 100 meters. The underlying structure of the crust is not exposed on the west side of the ridge as it is on the east. A large collapse or lava pond with delicate lava pillars was observed ~4.5 km west of the cleft (Figure 17d framegrab, west flank).

7.4. Southern Terminus (Dives T177, T178, T179, T457, T460, T735)

[35] Six ROV dives were completed at the southern terminus of the ridge axis that curves eastward into and around the westernmost end of Blanco Transform Zone. Dives T178, T179, and T457 examined the axis and eastern CBR 8–10 km north of the transform wall (Figures 2 and 18). Dive T460 includes a long transect from the axis across the western CBR to 5 km off-axis on the west side of the ridge. Dive T177 crosses the southernmost axial valley just north of the curved ridges of the RTI, which were subsequently explored and sampled on dive T735 (just south of area shown in Figure 18). There is a morphological transition from the southern cleft vent (SCV)-area (44°39′N) to the southern terminus of the segment (Figures 2 and 3): the floor of the axial valley deepens slightly by about 30 m, the "cleft" disappears (as does hydrothermal activity), the width of the axial valley increases from 2 km to 3.2 km, and the ADZ becomes broader and better defined (Figure 3). Here the inner rift floor is covered with semicontinuous massive flows that pond against and surround pieces of older faulted seafloor that comprise the inner edges of the ADZ. Compared to axial lavas to the north, the most evolved compositions were recovered in the axial valley on these ROV traverses.

[36] Within the southern terminus there are well-defined ridge-parallel fault slivers that delineate the

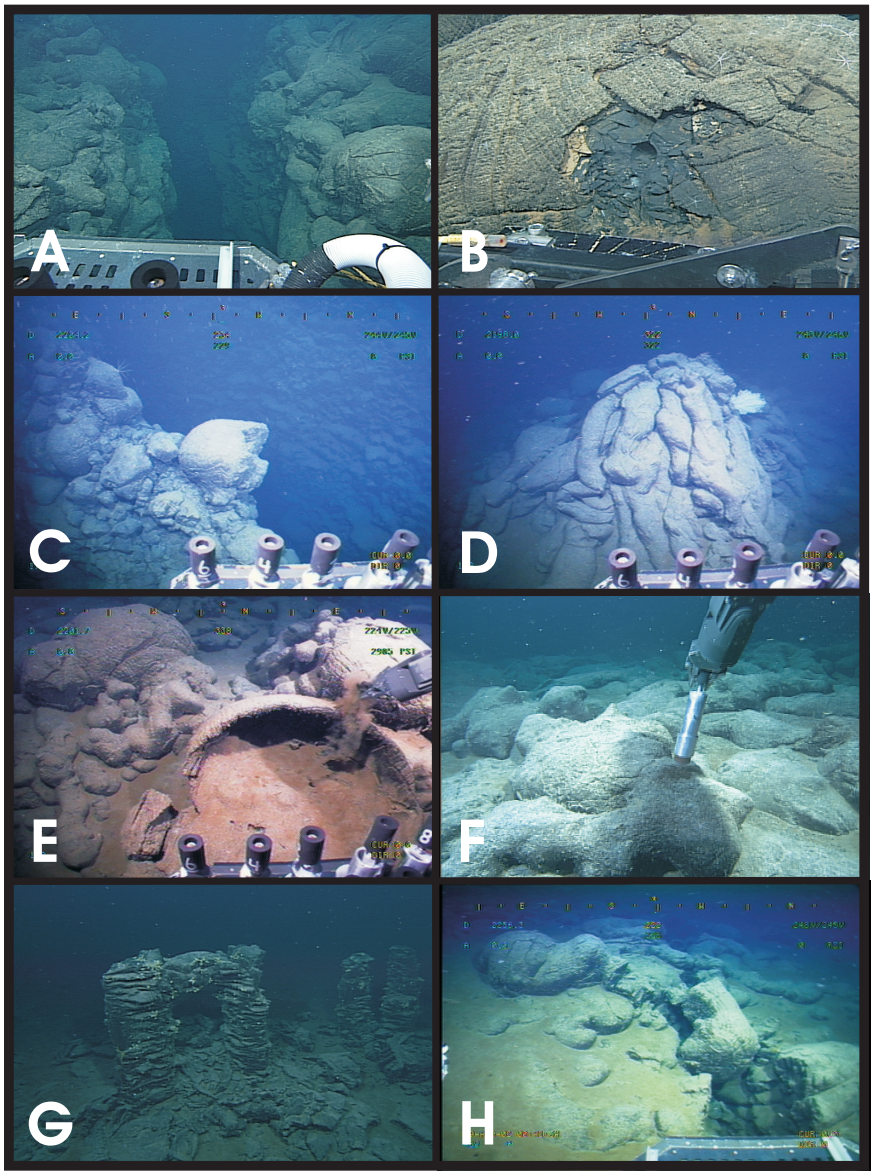

Figure 19. Selected framegrabs from T177, T178, T179, and T460. (a) T177: eruptive fissure with ramparts of fresh-appearing pillows (near T177-G4). (b) Andesite pillow sampled by ROV drill (borehole is 1.2″ in diameter) and recovered core is T177-G10 shown in Figure 18. T179: (c) open fissure and (d) haystack within eastern ADZ and crestal boundary ridge and (e) drained pillows on toe of flank pillows. T460: (f) unfaulted pillows of the western CBR, (g) collapse structures of perched lava lake within western ADZ, and (h) eruptive fissure decorated with evolved pillows on western CBR.

inside boundaries of the ADZ (Figures 2 and 18). These ridges have various morphologies that could be described as fault blocks, tilted massive flows, or horsts, and they are composed of heavily fissured crust that is visually older than the surrounding lobate and sheet flows (similar to what is described above in the Southern Section). In some places along Dives T178 and T460, folded and jumbled sheet flows are domed into pressure ridges covering the fault blocks. The series of scarps within the eastern ADZ (T178) are knife-edge fault bounded ridges, partially buried in talus. Unlike the central portion of the southern Cleft, the veneer of young sheet flows is incomplete at the southern terminus; critical exposures provide windows into the underlying faulted crust. The eastern ADZ (Dive T179) includes spectacular open fissures and haystacks (Figures 19a, 19c, and 19d) with flows partially draping fault talus. Two topographic knolls in the center of the axial valley (Dive T178, Figure 18) are pillowed mounds of FeTi basalt to ferroandesite. On Dive T177, the

ROV drillsled recovered cores from two bulbous pillows aligned with the ADZ fissures and fault systems (Figures 18 and 19b) that also proved to be ferroandesites (MgO < 5 wt%). These large bulbous pillows are not faulted and appear to have been extruded from local fissures along the inner edges of the ADZ (Figure 18). The andesitic pillows recovered near the southern terminus are unusual for MOR settings except at ridge transform intersections [see *Sinton et al. 1983*]. They appear to be a continuation of andesite ridges and giant pillow mounds (GPM, Figure 3) that form the curved ridges that form the northwestern wall of the West Blanco Deep (Figures 1, 2, and 3). Further to the west on dive T735 we found some of these hooked ridges are decorated by mounds, knobs, and domes of young-looking blocky lavas and pillows of andesite and dacite [*Cotsonika et al.*, 2005].

[37] The volcanic and tectonic structures observed on the western side of the axial valley, are repeated to a certain extent on the eastern CBR flank traversed on dives T178 and T179 where the terrain is predominantly covered with intact and unfractured, pillowed flows elongated downhill toward the east (Figures 18 and 19e). This constructional volcanic terrain on the ridge flanks strongly contrasts to the heavily faulted and fissured terrain found within the adjacent ADZ. Similar to the Dive T181, observations during Dive 460 showed that the western ADZ is bounded on the axis side by a ridge-parallel horst block that separates a perched eruptive center from the main young lava flow sequence. This eruptive fissure contains delicate lava pillars with uncollapsed arches that imply local eruption within the ADZ (Figure 19g). West of the intact eruptive center, the ADZ terrain has numerous faults aligned with small young-looking pillow mounds (Figure 19h) that coalesce into an unfaulted pillowed terrain (Figure 19f).

8. Lava Geochemistry and Distribution

[38] Major element compositions of 214 natural glass samples recovered along the southern Cleft and western Blanco Transform during this study (auxiliary material, 2005gc001038-ts01.txt) as well as all of the preexisting published geochemical data from this area (mostly from the axial valley) are used to investigate the spatial distribution of lava compositions along and across the southern Juan de Fuca Ridge. Off-axis regions of intermediate-spreading rate ridge segments have rarely been sampled as extensively or on such a fine scale as in this study and our data provide a relatively unique look at the spatial variability of the volcanic events as the crust moves away from the axis. Due to the axis-normal nature of our ROV traverses and the limited amount of time available for each dive, we were not able to distinguish individual lava flows with certainty. However, using contact relationships, structural features (e.g., fissures, haystacks built on top of faults or older flows), and differences in apparent age (i.e., sediment cover and glassiness of lava surfaces), we were sometimes able to infer sections of seafloor that differ in age by 100s to 1000s of years. The following discussion provides a broad discussion of the overall regional geochemical features of the Cleft axial valley and off-axis crust out to ~5 km.

[39] All of the lavas recovered during this study, as well as in previous studies, are N-type MORB with low K/Ti values that correspond to similar low values of incompatible element ratios (e.g., $Ce_N/Yb_N < 1$ and Zr/Y < 4 [*Smith et al.*, 1994; M. R. Perfit et al., manuscript in preparation, 2006]. Similar and relatively constant incompatible element ratios coupled with uniformly unradiogenic Sr and Nd isotope ratios are consistent with parental melts derived from a relatively homogeneous incompatible element-depleted mantle source with little variation in the extents of melting. Major elemental variations (with the exception of some highly evolved andesites and dacites that show evidence for magma mixing) can be modeled by low-pressure (~100 MPa) fractional crystallization (up to ~80%) [*Smith et al.*, 1994; *Tierney*, 2003]. Consequently, the abundance of MgO in each sample can be used as an indicator of the extent of magmatic evolution and thus the distribution of lava compositions can be related to such factors as the thermal evolution of the ridge and temperature regimes in the AMC (see discussions by *Sinton and Detrick* [1992] and *Sinton et al.* [2002]). A positive correlation between MgO and the cross-sectional area of fast spreading ridges has led to the belief that inflated ridges generally erupt higher temperature magmas that are supplied more rapidly to the ridge axis [*Scheirer and Macdonald*, 1993; *Macdonald*, 1998]. Although this hypothesis has not been substantiated on intermediate-rate spreading ridges we make the assumption here that robust magmatism, characterized by frequent magmatic events or recharge, leads to the eruption of greater volumes of lava (not necessarily larger flows), which have higher MgO contents (i.e., more primitive compositions (see *Rubin et al.* [2001] for discussion). Conversely, waning magmatism leads

to less voluminous flow units with lower MgO contents (more evolved) and possibly more heterogeneous compositions. Along the southern JdFR lower MgO lavas are most likely generated by the cooling and crystallization of higher MgO, more primitive magmas. This might result as a consequence of (1) less frequent mantle recharge events in a cooling magma chamber or lens [*Macdonald*, 1998], (2) more enhanced cooling of the AMC due to increased hydrothermal circulation as a consequence of increased faulting and fracturing of the crust [*Phipps Morgan and Chen*, 1993], and (3) tapping the cooler edges of a magma body or lens [e.g., *Perfit et al.*, 1994] or rift propagation/diking into cooler crust [e.g., *Sinton et al.*, 1983].

[40] MgO abundances along the Cleft Segment range from 1.13 wt.% to 10.53 wt.%. However, the most evolved sample, a dacite, RC 10 was collected by rock core from an area of curved volcanic ridges at the RTI, and the most primitive basalts (>9.7 wt.% MgO), were collected from a small seamount (Dive T461; SM in Figure 15) on the western side of the southern Cleft. Excluding these locations and including all available data from the southern Juan de Fuca Ridge, the range of MgO varies from around 9.3 in normal basalts to around 3 wt.% in ferroandesites (average and median of 376 samples from on and off-axis are ~7.0). In general, there is a southward decrease in MgO contents of the lavas, consistent with the dredge data [*Sinton et al.*, 1983] and observations of *Smith et al.* [1994] based solely on basalts recovered in the axial valley.

[41] To interpret the geochemical distribution on a finer scale, the Cleft Segment was divided into 6 different morphotectonic regions. From south to north these areas are (1) the ridge-transform intersection (RTI) (from 44°27′N to 44°30′N); (2) the axis of southern Cleft Segment from 44°30′N to 44°50′N; (3) S. Cleft off-axis, (east and west of the axis from 44°30′N to 44°50′N); (4) the axial region of the northern Cleft Segment from 44°50′N to 45°05′N, (5) N. Cleft off-axis, east and west of the axis; and (6) the region north of N. Cleft where it overlaps with the Vance segment (OSC/Vance from 45°05′N to 46°55′N). Additionally, comparisons are made between the entire Cleft axial region and those off-axis regions to the east and west from 44°30′N to 45°05′N.

[42] Because excellent correlations exist between MgO concentration and most other major and minor elements in the glasses and because MgO can be used as a proxy for magma temperature and hence degree of evolution, we have chosen to compare the different regions on the basis of their mean and average MgO contents (Table 3). The numbers of lavas located within the RTI and the OSC/Vance regions do not include significant numbers of off-axis samples. Consequently all of the samples recovered from these two areas are included in the subsequent discussion.

Table 3. Regional MgO Variations in Lavas Along the Southern JdFR

Region	MgO Average, wt.%	MgO Median, wt.%
Axial Samples Only		
S. Cleft Young Sheet Flow	6.94	6.99
N. Cleft Young Sheet Flow	7.61	7.60
All Samples (On- and Off-Axis)		
Ridge Transform Intersection (RTI)	5.92	6.30
Southern Cleft	6.74	6.86
Northern Cleft	7.54	7.63
N. Cleft Overlap Zone (OSC) with Vance Segment	7.98	8.21
Northern Cleft + Southern Cleft (Western side)	5.93	6.57
Northern Cleft + Southern Cleft (Eastern side)	6.92	6.97

[43] There is a distinct trend toward more evolved samples as the RTI is approached. The most recent young sheet flows that fill the axis at both north and south Cleft also conform to this trend (Table 3) [*Smith et al.*, 1994]. Median abundance values of MgO wt.% in glasses from each of the regions defined above from north to south are: 8.21 (OSC/Vance), 7.63 (northern Cleft, including on and off-axis samples), 6.86 (southern Cleft, including on- and off-axis samples), and 6.30 (RTI) (Table 3). Overall, the OSC/Vance and the northern Cleft Segment contain the greatest number of relatively primitive lavas compared to the southern Cleft Segment and the RTI where lavas as evolved as dacite have been recovered [*Cotsonika et al.*, 2005]. Grouping lavas into bins of 1 wt% MgO the geochemical data show the percentage of lavas between 8.0 and 9.0 wt.% MgO from the OSC/Vance is approximately 70% and the percentage of lavas between 7.0 and 8.0 wt.% MgO from the northern Cleft Segment is approximately 68%. The greatest percentage of the lavas from the southern Cleft Segment and RTI contain between 6–7 wt.% MgO (~53% and ~41%, respectively) (Figure 20). None of the samples collected from the northern Cleft and Vance segments contain less than ap-

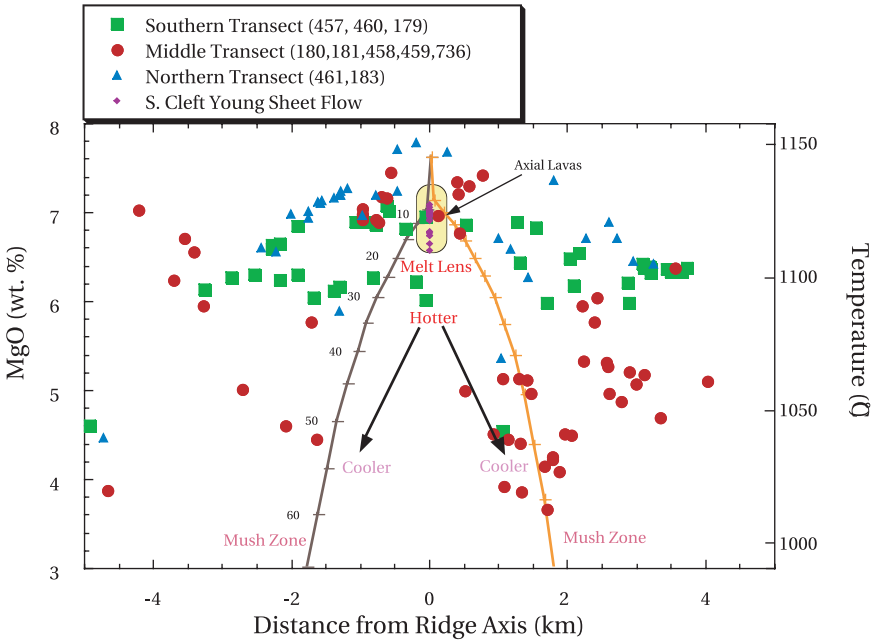

Figure 20. Across-axis chemical variation (MgO wt.%) in S. Cleft lavas recovered by ROV during this study. Glass analyses (provided as auxiliary material; M. R. Perfit et al. manuscript in preparation, 2006) show the more evolved nature of off-axis lavas and the greater range in compositions compared to the samples recovered from in the axis and the youngest flows in the axis (S. Cleft Axial flows; yellow oval represents the average composition ± 2-sigma s.d.). The colored symbols represent lavas from various combinations of east-west ROV dive transects in the northern (green squares), middle (red circles), and southern (blue triangles) sections. The specific dive numbers are listed for each transect. High-MgO samples from a near-axis seamount (T461) and andesites from near the RTI (T177, T178, T735) have not been plotted on the diagram (no AMC was detected by *Canales et al.* [2005] where these dives are located). Superimposed on data are representative calculated curves showing the variation in MgO content in residual liquids (brown curve on west side of axis) as a result of fractional crystallization of one of the more primitive axial lavas (MgO = 7.8 wt. %). Numbers on curve represent percentage of crystallization of the parental magma containing 0.25 wt.% H2O at 1 Kb pressure. Calculated magma temperatures (orange curve) are shown on the right side of the diagram. Because temperature distribution within the crust along the Cleft is unknown and would change as the balance between magma input and hydrothermal cooling changed, the temperature-distance curve is meant to be illustrative. Temperature and melt distributions of AMC in general are not well known but here were estimated from models of the northern EPR [*Crawford and Webb*, 2002; *Maclennan et al.*, 2005]. Along the southern Cleft south of 44°50′, AMC widths vary from approximately 800 m (south and north) to 1600 m (middle) [*Canales et al.*, 2005]. The distribution of lavas is consistent with a model that suggests the axial flows are derived from the hotter, less crystalline center of the melt lens while more evolved lavas recovered from the flanks are derived from the cooler, more crystalline edges of the AMC or the mush zone.

proximately 6.0 wt.% MgO, and overall the northern Cleft Segment (average MgO = 7.54 wt.%,) is significantly more primitive than the southern Cleft Segment (average 6.74 wt.%) (Table 3).

[44] Partly on the basis of the nonsteady state model of *Kappel and Ryan* [1986], *Smith et al.* [1994] suggest that lavas from S. Cleft differ from those at N. Cleft because the S. Cleft is in a more mature magmatic stage dominated by tectonism and the eruption of more evolved (cooler) magmas. However, this tectono-magmatic model hypothesized that the crestal ridges (CBR) might be composed of more primitive (hotter) lavas erupted during a more robust magmatic episode. Although our morphologic and tectonic observations are consistent with this hypothesis, our geochemical data show that on average, the lavas recovered from the CBR and off-axis at S. Cleft actually have lower MgO than axial lavas; opposite to what might be expected from MgO versus ridge morphology arguments discussed above. Comparing samples from the floor of the S. Cleft axial valley, where we can be very certain the lavas are young and locally erupted, to those recovered off-axis, outside of the axial valley, MgO abundances average 6.94 wt.% (the mean is 6.99 and the s.d. is 0.13) within the axial valley compared to those from off-axis sites that average 5.78 wt.%. The

more variable and evolved compositions further away from the axis are shown in Figure 20. Similar spatial variations in lava compositions away from the axis have been noted around 21°N on the EPR [*Hekinian and Walker*, 1987] and in the FAMOUS area on the MAR [*Bryan and Moore*, 1977]. More recent and detailed studies of the 9°–10° N section of the EPR have also documented a greater extent of differentiation and chemical variability in off-axis lavas compared to those in the present axial region [*Perfit et al.*, 1994; *Perfit and Chadwick*, 1998].

[45] The highly variable and nonsystematic compositions of the off-axis lavas at the Cleft Segment (eastern side, 4.46 to 8.54 wt.% MgO, western side (excluding samples from a small seamount); 3.20 to 7.48 wt.% MgO) are difficult to reconcile given the documented homogeneity of lavas in the S. Cleft axis [*Smith et al.*, 1994; M. R. Perfit et al., manuscript in preparation, 2006]. Assuming all magmatism was focused within the axis of the Cleft over the past 50 kyr or so, and that magmatic activity has been waning with time, lavas further to the east and west of the axis should be systematically more primitive with characteristics of more high effusion rate eruptions (e.g., more sheet/lobate flows and drained lava lakes) and possibly more homogeneous compositions over small spatial scales. We see, however, quite the opposite; lavas dominated by pillows with highly variable, more evolved compositions. In addition it is unclear why lavas from the western side of the axis would be more fractionated on average than the eastern side (5.93 versus 6.92 wt% MgO) if spreading was symmetrical and/or the erupted lavas were sourced from a more or less central axial vent system. These observations are significant because they suggest asymmetric accretion or that off-axis magmatism is an important process that dominates the volcanic features and compositions away from the axial valley.

9. Discussion

[46] *Kappel and Ryan* [1986] describe south Cleft as a single linear volcano with eruptions pouring out up to 10 km from axis. They note the flat-lying lavas that fill the axial valley are younger and more faulted and fissured than the coherent flows that comprise the flanks of the ridge that they hypothesized formed during a robust period of volcanism. Their hypothesis is mostly based on bathymetric and side scan data. *Smith et al.* [1994] proposed a tectono-magmatic model that also relied on the episodic nature of magmatism along the Cleft Segment primarily but uses observations and samples recovered in the axis of the southern JdFR and some off-axis dredges. The types of magmatic cycles proposed may not just characterize the JdFR as it has been suggested that waxing and waning magmatic phases also occur along the EPR [*Fornari et al.*, 1998; *Cormier et al.*, 2003].

[47] Prior to this study nearly all of the geologic observations and petrologic studies had been made on-axis in the neovolcanic zone and not of the CBRs or, in fact, along the faulted walls of axial valley. Below we discuss the various lines of evidence we have gathered that argue against the episodic split-ridge hypothesis first outlined by *Kappel and Ryan* [1986] and attempt to reconcile our results based on recent seismic reflection work completed along the JdFR [*Canales et al.*, 2005; *Carbotte et al*, 2006]. The data help reveal how crustal accretion has occurred along the Cleft Segment over the recent past (<400 kyr).

9.1. Geological and Geochemical Constraints on Crustal Construction

[48] Recent magmatism along the Cleft Segment has likely occurred by eruptive fissuring over a narrow axial magma lens and down-rift lateral dike injection [*Embley and Chadwick*, 1994]. Two decades of study of the Cleft Segment has focused on samples collected from the youngest flows within the axial rift valley that likely represent the products of several periods of recent (last few decades) eruptive activity [*Normark et al.*, 1986; *Smith et al.*, 1994; *Smith*, 1999; *Embley and Chadwick*, 1994]. The results of these studies suggest that the axial valley is covered with moderately evolved, incompatible element-depleted basalts (N-MORB) with relatively small chemical variations that are consistent with the effects of shallow-level fractional crystallization [*Dixon et al.*, 1986; *Smith et al.*, 1994; M. R. Perfit et al., manuscript in preparation, 2006]. On the basis of the systematic latitudinal changes in composition of the axial lavas, *Smith et al.* [1994] proposed that the Cleft Segment goes through cycles that vary from robust magmatism typical of fast spreading centers with well-focused, narrow, "steady state" zones of primary crustal accretion to periods of mostly amagmatic extension with poorly focused, intermittent volcanism similar to that occurring along slower spread ridges. This model predicts that if the lavas that form the CBR were erupted on-axis (from the "cleft") during a period of robust mag-

matism, they would have a primitive basaltic (high-MgO) composition, which they do not. Off-axis samples, particularly from the CBR, are moderately to highly evolved (ferrobasalt to FeTi basalt) but also include a few ferroandesites. The range of compositions is greater than that previously reported for the entire southern JdFR and distinctly more evolved than the young lavas erupted in the axis [*Perfit et al.*, 2003]. Lavas sampled in cross-axis traverses encompass the entire range of compositions with no readily discernable pattern of variation with distance from the axis nor are the chemical trends symmetrical across the ridge crest; features which are inconsistent with previous tectono-magmatic hypotheses [*Kappel and Ryan*, 1986; *Smith et al.*, 1994]. *Pollock et al.* [2005] see similarly large variations in basalt chemistry in samples collected from the north wall of the Blanco Transform Zone. Their inferred stratigraphy, based on limited sample recovery, however, suggests that older, stratigraphically lower lavas are more evolved than younger higher-MgO lavas, which is not immediately correlative with the regional distribution observed in our surficial off-axis samples.

[49] Within each transect across axis, the more evolved compositions (andesites and FeTi basalts) are more commonly, but not exclusively, associated with haystacks and small pillow mounds as well as the perched lava lakes that are found within or proximal to the ADZ. Along the traverse of Dive T181, the more fractionated magmas were found in eruptive fissures within the ADZ or on the western CBR. Further south, on Dive T177, large ferroandesite pillows recovered within the axial valley are associated with small pillow mounds and recently active faults bounding the axial floor. Although most of the major and trace element chemical variability can be explained in terms of low-pressure fractional crystallization of N-type parental magmas with compositions similar to recently erupted axial MORB, the most highly fractionated andesites and dacites require extreme amounts of fractional crystallization as well as additional processes (mixing/crustal assimilation) to explain their unusual compositions [*Cotsonika et al.*, 2005; M. R. Perfit et al., manuscript in preparation, 2006]. The overall distribution and chemistry of the lavas are inconsistent with their having formed from a single linear volcano, and instead we suggest that portions of the ADZ and the CBR (at least at the surface) were formed by magmas tapped from the cooler distal edges of an AMC (Figure 4). At present the top of the AMC has been determined to be 2 km wide [see *Canales et al.*, 2005], which places the edges of it just below the bounding faults and ADZ. Assuming the AMC reflector represents a concentration of melt at the top of a crustal magma body then it follows that its disappearance at the walls of the axial valley likely represents a transition to more crystalline or "mushy" zones that have lower temperatures and have crystallized to a greater degree than magmas in the central eruptive zone [e.g., *Sinton and Detrick*, 1992; *Perfit and Chadwick*, 1998].

[50] The moderately to highly fractionated lavas of the ADZ and CBR are interpreted as syntectonic eruptions as proposed by *Macdonald et al.* [1996] to explain similar off-axis features on the northern EPR [*Perfit et al.*, 1994; *Sohn and Sims*, 2005]. In this model, abyssal hills are bounded on both sides by normal faults, but on the side facing away from the ridge the faults are draped by lava flows that are mainly intact elongate pillows. Such "volcanic growth faults" form in a "flanking tectonic province" 2–6 km from the ridge axis, and are repeatedly covered by syntectonic lava flows [*Macdonald*, 1998].

[51] *Buck and Poliakov* [2005] suggest faulting associated with the formation of an axial valley may go through an evolutionary process with initial faults dipping toward the ridge axis and those formed later dipping away from the axis. This faulting and development of an axial valley are a consequence of lithospheric stretching and extension that is not tied to temporal variations in magmatism. We propose that off-axis eruptions are related to extensional faults and fissures breaching the underlying magmatic system away from the axial neovolcanic zone. Concentrations of melt in the lower crust can also create stress regimes that focus dikes up to a few km from the axis [*Fialko*, 2001]. *Sim et al.*, [2004] and *Sim* [2004] suggest that when a magma lens is pressurized as a result of fresh magma input, subsequent diking will tend to occur near the tips of the lens (the distal edges of the chamber). In their model these dikes tend to propagate nearly vertically toward the surface, where their location relative to the ridge axis reflects the size and relative location of the magma lens. Within the ADZ, and on the summit of the CBR, open fissures and small fault-related steps partially covered by pillows and eruptive fissures filled with fractionated lavas are consistent with this concept. In addition, the remarkably coherent (little or no faulting) nature of the CBR, particularly compared to the "younger" intensely faulted

ADZ, strongly supports a sufficient volume of off-axis volcanism to cover preexisting faults. There is another type of off-axis volcanism; one associated with the development of small, near-axis seamounts composed of quite primitive lavas (e.g., T461; see Figure 16). In aggregate, these constructs are not as volumetrically significant as the other styles of off-axis volcanism, but are important components of off-axis crust. We suggest that 150–250 m of lava must be added to the flanks of the spreading center within 2–3 km of the axis as the observed perched lava lakes, haystacks, fissure-fed flows, small seamounts and the prominent pillow lava flows that comprise most of the CBR.

[52] Our model is also consistent with that of *Carbotte et al.* [2006], who propose that dike intrusion alone, unrelated to tectono-magmatic phases, will lead to the progressive rifting, deepening and widening of JdF axial valleys. Their evolutionary model allows for the zone of deformation to become localized along graben-bounding faults (analogous to the ADZ) that deepen as tensile stresses from dike propagation from the magma lens continue. This could result in early mafic volcanism focused at the central axis followed by more chemically evolved off-axis volcanism as the zone of deformation zone becomes wider and extends deeper.

[53] Submersible observations of 0.8 to 1.2 Ma rock exposures along the northern wall of the West Blanco transform reveal that in cross-section the oceanic crust can be divided into an upper relatively intact, undeformed section of pillow and lobate lavas that overlie more massive and strongly jointed lava crosscut by feeder dikes [*Juteau et al.*, 1995; *Tivey et al.*, 1998; *Karson et al.*, 2002]. Magnetic data identifying the reversal polarity stratigraphy in cross-section at the West Blanco transform also indicate the uppermost lavas have a shallower dip than the deeper lavas, which implies that upper lavas either flowed or erupted several kilometers from the axis [*Tivey et al.*, 1998]. This latter point is compatible with the ROV observations and morphology data that show the edge of the most recent CBR are some 3 to 5 km off axis. The uppermost lavas represent not only the youngest lavas but also those that flowed the greatest distance from or erupted away from the axis. The deeper portions of the extrusives are older and represent lavas erupted on-axis that have been subsequently fractured, intruded, buried and tilted toward the axis [*Tivey et al.*, 1998; *Karson et al.*, 2002]. Although sampling in the transform was on a coarser scale than our ROV sampling, the upper 200 m shows a transition from less to more primitive lavas [*Pollock et al.*, 2005]; opposite to the trend expected from our results. Few in situ stratigraphic sections of undisrupted of oceanic crust have been studied to date [*Karson*, 2002] and geochemical data from ODP/DSDP holes in the Pacific (e.g., 504B, 1224, 1256) show trends of both increasing and decreasing MgO in uppermost lavas. Consequently, evidence for systematic changes in lava geochemistry either from off-axis or waning stages of volcanism are lacking from other sites.

9.2. Geophysical Evidence for Crustal Construction

[54] The composite ROV magnetic profiles across the Cleft axis are all well within the Brunhes normal polarity chron and so any variations in crustal magnetization we observe are either due to magnetization intensity or source layer thickness changes. Looking at magnetization intensity first, we have produced a simple linear spreading model of Earth's paleointensity over the past 100 kyr based on the relative paleointensity record of *Guyodo and Valet* [1999] combined and matched with the archeomagnetic data of *McElhinny and Senanayake* [1982]. Examining the correlation between the paleointensity record and the profiles (Figure 13) we find a remarkable correlation with the axial magnetic high. If this is the case then the axial lavas likely represent an age span of some 0-4000 years while those at the edge of the axial valley could be up to 35 kyr in age, which is compatible with the average spreading rate for this area.

[55] The central cleft magnetic transect (T183 and T461) has a more box-like signal over the axial valley with sharp transitions at the edge of the valley compared to the triangular magnetization highs on the southern transects. This is consistent with observations that the entire inner valley floor is filled with young lavas. To the south, the lavas are not as voluminous and are more localized and limited to their eruptive centers giving rise to the more triangular magnetization pattern. This magnetic signature might therefore reflect the robustness of the axial volcanic system toward the north. Outside of the inner axial valley floor there is a correlation between the paleointensity record and observed flank anomalies over the CBR (Figure 13). While it is tempting to attribute the entire signal to the paleointensity signal we know

there are systematic variations in seismic layer 2A thickness, especially beneath the CBR [*Canales et al.*, 2005]. Seismic layer 2A shows that the flanking CBR are ~600 m thick while the axial valley is only half as thick, i.e., 200 to 300 m thick. In light of these data, the strong magnetizations found over the CBR are likely to be associated with thicker layer 2A relative to the thinner crust at the axis rather than more strongly magnetized material. Interestingly, the CBR have sharp boundaries in magnetization at their distal outer edges (at ~3 km) as well as at their inner boundaries relative to the axis. Following the lava emplacement modeling of *Schouten et al.* [1999], this outer edge could be interpreted as the edge of the extrusive lava thickening zone where layer 2A thickness attains mature and constant thickness, i.e., the distal edge of lava transport. Such an interpretation is compatible with the magnetic results from the Blanco Transform Zone [*Tivey et al.*, 1998], which found that the upper lavas extend between 3 and 4 kilometers away from the axis of spreading during accretion. Morphological data also support the observations of lava deposition or eruption several kilometers away from the axis. Furthermore many of the off-axis flows associated with fissures and the constructional mounds and haystacks are composed of highly evolved ferro- and FeTi basalts that have intrinsically high magnetizations. If the thicknesses of these highly magnetized flank flows are on the order of a few hundred meters this would produce significant local anomalies consistent with the amplitudes we observe.

[56] New multichannel seismic reflection data from the southern JdFR show about 60% of the Cleft Segment is underlain by an AMC that deepens from ~2 km beneath the south cleft vents (SCV) to ~2.3 km at north cleft [*Canales et al.*, 2005; *Carbotte et al.*, 2006]. An AMC reflector is not present south of 44°38′N; just to the north of our southern ROV transects at ~44°35′N. Seismic layer 2A nearly doubles in thickness from about 200–300 m to 600 m off-axis with most of the thickening occurring at the walls of the axial valley (ADZ) and reaching full thickness 3–4 km from the axis (analogous to the base of the CBR). The seismic data conclusively show the southern Cleft is magmatically active and not in a tectonic state. *Canales et al.* [2005] propose a "thermal" model where subtle changes in magma supply control the topography of the Cleft axis. Their model predicts the ridge would progress from an inflated EPR-like axial high to the current configuration with a well-defined, deep axial valley as a consequence of decreased magma input. It is unclear, however, why a shallower AMC reflector and thinner crust in the south correlates with the most recent eruption of more evolved lavas compared to the higher-MgO lavas at north Cleft and Vance where the AMC is deeper and the crust is thicker. It is unlikely that the variations in axial thermal structure are due to changes in mantle melt productivity since there are no suggestions in the isotopic or trace element chemistry of the southern JdF lavas that the mantle has either had some compositional or thermal change over the past ~0.5 ma (M. R. Perfit et al., manuscript in preparation, 2006). In the *Canales et al.* [2005] model, the bounding ridges (our CBR) are formed as a consequence of flexural uplift and covered with flows emanating from a central axial rift during increased magma supply. On the basis of geochemical arguments presented above, this would likely result in the CBR being composed of relatively high-MgO lavas, contradictory to what we observe. *Carbotte et al.* [2006] show that axial grabens along the entire JdFR become shallower and narrower where AMC reflectors disappear and suggest axial rift topography is related to magma-induced deformation rather than tectono-magmatic cycles. They propose that dike intrusion alone, will lead to the progressive rifting, deepening and widening of JdF axial valleys. Their evolutionary model allows for the zone of deformation to become localized along graben-bounding faults (analogous to the ADZ) that deepen as tensile stresses from dike propagation from the magma lens continue. In this model the bounding ridges are relicts of an evolutionary model that begins with the formation of an axial volcanic ridge (AVR) that are subsequently split by dike-induced faulting and rafted onto the ridge flanks. Although early volcanism created at the central axis would be relatively unfractionated it could be followed and covered by more chemically evolved off-axis volcanism as the zone of deformation zone becomes wider and extends deeper to tap magma on the edges of the AMC.

[57] Both models indicate the flanks of the ridges (our CBR) would be thickened by lavas flowing down and away from the axial highs before a deep axial graben forms that would limit flows from leaving the axis. This process is similar to that suggested on the NEPR [e.g., *Hooft et al.*, 1996; *Fornari et al.*, 2004; *Soule et al.*, 2005]. However, it should be noted that even on the present robust NEPR, the distribution of flows from the axis up to a few km off-axis appears to have been accomplished by lava moving along narrow flow

channels that form distinct sheet and lobate flows which are not present on the Cleft CBR. Off-axis pillows on the EPR are found either at flow fronts or as ridge axis-parallel pillow mounds that erupted off-axis [*Perfit and Chadwick*, 1998; *Soule et al.*, 2005].

[58] Although fast spreading ridges like the EPR do not have large axial valleys or graben it is important to note that models for the development of axial summit troughs are similar in many respects to those presented here for the JdFR. Most involve cyclic changes in the supply of magma to the ridge crest whereby waning magmatic activity is associated with increased fissuring and faulting, structural collapse of the crust, widening of the axial caldera or collapse trough, small volume eruptions and some off-axis volcanism [*Fornari et al.*, 1998; *Lagabrielle and Cormier*, 1999; *Cormier et al.*, 2003].

10. Conclusions: Construction of the JdFR Along the Cleft Segment

[59] Previous studies of the intermediate spreading rate Cleft Segment [e.g., *Kappel and Ryan*, 1986;] have suggested that this segment oscillates between "fast-spread" and "slow-spread" crust, with morphological similarities to each spreading regime during different periods of time. On the basis of the morphology provided by the EM300 data, we initially hypothesized that the Cleft was a "split ridge" with the CBR formation linked to periods of robust magmatism as suggested by *Smith et al.* [1994] after *Kappel and Ryan* [1986]. Although the "split-ridge" model for intermediate ridges offers a simple and compelling explanation of the regional structures, we are forced to reject it on the basis of our detailed geological, geochemical and magnetic data from the Cleft Segment coupled with the recent multichannel seismic results discussed above.

[60] Our results reveal the structural, petrologic and magnetic complexity of the uppermost crust of ocean crust that comprises the Cleft Segment of the JdFR. Particularly striking are the differences in structure, lava morphology and commonly, lava geochemistry between the axial valley, axial disrupted zone (ADZ), and the flanking crestal boundary ridges (CBR). We suggest that oceanic crust formed at this intermediate spreading rate ridge represents a balance between the magma supply and the regional extension. Unlike fast-spread crust, the magmatism is inadequate to sustain a robust thermal and magmatic center that is not impacted by the regional extension. Unlike slow-spread crust, the magmatic budget is robust enough to preclude long episodes of amagmatic extension at the axis with extensive tectonic deformation. On the Cleft Segment, the balance is such that replenishment of new magma is frequent enough to overcome hydrothermal cooling to maintain an AMC but allows for shallow-level crystal fractionation to govern and modulate the distribution of magma types on the axis (Figure 20). However, extensional forces apparently exceed magmatic supply within a few kilometers of the spreading axis such that tectonic breaching, possibly enhanced by diking, of the AMC is common.

[61] The tectonic dismemberment of the newly formed crust in the axial disrupted zone (ADZ) permits melts from the edges of the AMC to be erupted within 2–3 km of the axis and to create at least the uppermost portions of crestal boundary ridges (CBR). Eruptions from a "breached magma chamber" generate a magmatic/tectonic evolution with lower lavas generated from the central part of the magmatic system, which are capped by more fractionated and heterogeneous lava erupted off-axis along fissures and faults from cooler, more evolved portions of the magma body (Figure 20). The more evolved magmas may be from the cooler distal edges of the melt lens or from the more crystalline sections of the mush zone that must exist away from the central axis similar to what has been proposed for the NEPR [*Perfit et al.*, 1994; *Fornari et al.*, 1998]. Lavas that erupt from the leaky flanks are spatially related to the faults that bound the abyssal hills perhaps related to bending or stretching of the lithospheric plate [e.g., *Sohn and Sims*, 2005; *Buck and Poliakov*, 2005] or dike-induced graben formation [*Carbotte et al.*, 2006]. We suggest that this process can explain a significant proportion of off-axis thickening of Layer 2A documented by the seismic survey of the Cleft Segment [*Canales et al.*, 2005]. Further from the axis, the crust is crosscut by ridge-parallel faults and fissures that are ubiquitously decorated by mounds and haystacks of volcanic material. The ridge parallel structures are offset by ridge-oblique structures on the flanks of the spreading axis. The oblique orientation, orthogonal to the direction of regional plate spreading signals the transition from the magmatic near-axis system to the syntectonic flank system in which the formation of extensional crustal structures provides pathways for residual magma and concomitant local hydrothermal fluid venting. The different fault orientations appear to

reflect a change in the structural regime from one dominated by ridge-parallel extensional faults and fissures associated with a robust volcanic system to a tectonic regime in which the regional plate motion dismembers the upper oceanic crust and provides pathways for later intrusions, eruptions and hydrothermal flow. Magnetic profiles across the spreading axis are consistent with both (1) the thickening of the upper crust by the off-axis formation of the CBR and (2) the local off-axis eruptions of more evolved lavas.

[62] We offer a new model for crustal development along the Cleft Spreading segment based on our observations and that incorporates some of the new results from JdFR seismic studies. We hypothesize a magma-chamber modulated cycle of crustal formation with more primitive and homogeneous initial magmatism focused along an axial rift followed by lesser volumes of heterogeneous and more evolved lavas that occur in a more diffuse zone within 2–3 km of the axis. The complete cycle includes a magma recharge event causing narrow axial eruptions, followed by widening of the zone of intrusion [e.g., *Carbotte et al.*, 2006] magmatic collapse (a breached magma chamber) within a few km of the spreading axis as the melt lens or sills are depleted in magma. This is supplemented by small volumes of flank eruptions >2–3 km (the leaky flanks). These three phases together build the crust at Cleft and are consistent with the observed thickening of layer 2A within a few kilometers of the axis.

Acknowledgments

[63] The data and samples for this study were collected during three extremely successful cruises with contributions from many people. The crew of the R/V *Western Flyer* and the pilots of the ROV *Tiburon* worked tirelessly to insure we completed all of our objectives. They were supportive and creative partners in the field program, and our success must be shared with them. We thank them for their efforts, skill, and good humor. A good number of scientist and students were also instrumental during the cruises, and we thank the following people for their help: Karen Salamy, Jenni Kela, Jim Gill, Frank Ramos, George Kamenov, Laurie Cotsonika, Sarah Langberg, Deborah Glickson, Geoff Wheat, Lonnie Lundsten, Bethany Schaarschmidt, Meg Tivey, Ed Delong, Peter Saccoccia, Josh Plant, Thomas Chapin, Kevin Gomes, Paul McGill, and Greg Moretti. We also wish to thank Karen Salamy, Jenni Kela, Trey Montgomery, Susan Tierney, Sarah Langberg, Jessica Tibbitts, Ian Ridley, and Robert Oscarson for analytical assistance. We would especially like to thank Annette Gough at MBARI for providing expertise in creating and managing the images and text files for this paper. Discussions with M. Smith, I. Ridley, J. Sinton, S. Carbotte, D. Smith, J-.P. Canales, and C. Chadwell regarding this research were extremely helpful and illuminating. This manuscript benefited greatly from careful reviews by W. W. Chadwick and J. Sinton. M. Perfit is grateful for the support and facilities provided to him by MBARI during his sabbatical. This research has been partially supported by a NSF grant to M. Perfit (OCE-0221541). M. Tivey acknowledges support from WHOI's Mellon grant for Independent Study plus Paul Fucile for sensor engineering and Deniz Kazanci for her initial workup of the magnetic data as a WHOI Summer Student Fellow. Support for D. Stakes, T. Ramirez, D. Caress, and N. Maher and for the entire field program was provided by funds to MBARI from the Lucille and David Packard Foundation.

References

Ballard, R. D., and J. G. Moore (1977), *Photographic Atlas of the Mid-Atlantic Ridge Rift Valley*, 114 pp, Springer, New York.

Baker, E. T., J. W. Lavelle, R. A. Feely, G. J. Massoth, S. L. Walker, and J. E. Lupton (1989), Episodic venting of hydrothermal fluids from the Juan de Fuca Ridge, *J. Geophys. Res.*, *94*, 9237–9250.

Baker, E. T. (1994), A 6-year time series of hydrothermal plumes over the Cleft segment of the Juan de Fuca Ridge, *J. Geophys. Res.*, *99*, 4889–4904.

Buck, W. R., and A. N. B. Poliakov (2005), Abyssal hills formed by stretching oceanic lithosphere, *Nature*, *392*, 272–275.

Bryan, W. B., and J. G. Moore (1977), Compositional variations of young basalts in the Mid-Atlantic Ridge rift valley near 36°49′N, *Geol. Soc. Am. Bull.*, *88*, 556–570.

Canales, J. P., R. S. Detrick, S. M. Carbotte, G. M. Kent, J. B. Diebold, A. Harding, J. Babcock, M. R. Nedimović, and E. van Ark (2005), Upper crustal structure and axial topography at intermediate spreading ridges: Seismic constraints from the southern Juan de Fuca Ridge, *J. Geophys. Res.*, *110*, B12104, doi:10.1029/2005JB003630.

Carbotte, S. M., and K. C. Macdonald (1994), The axial topographic high at intermediate and fast spreading ridges, *Earth Planet. Sci. Lett.*, *128*, 85–97.

Carbotte, S., M. R. S. Detrick, A. Harding, J. P. Canales, J. Babcock, G. Kent, E. Van Ark, M. Nedimovic, and J. Diebold (2006), Rift topography linked to magmatism at the intermediate spreading Juan de Fuca Ridge, *Geology*, *34*(3), 209–212.

Caress, D. W., and D. N. Chayes (1996), Improved processing of Hydrosweep DS Multibeam Data on the R/V Maurice Ewing, *Mar. Geophys. Res.*, *18*, 631–650.

Caress, D. W., D. N. Chayes (2005), MB-System: Open source software for the processing and display of swath mapping sonar data, Monterey Bay Aquarium Res. Inst., Moss Landing, Calif. (Available at http://www.mbari.org/data/mbsystem/)

Chadwick, W. W., Jr., and R. W. Embley (1994), Lava flows from a mid-1980s submarine eruption on the Cleft segment, Juan de Fuca Ridge, *J. Geophys. Res.*, *99*, 4761–4776.

Chadwick, W. W., Jr., R. W. Embley, and C. G. Fox (1991), Evidence for volcanic eruption on the southern Juan de Fuca Ridge between 1981 and 1987, *Nature*, *350*, 416–418.

Chadwick, W. W., Jr., R. W. Embley, and T. M. Shank (1998), The 1996 Gorda Ridge eruption: Geologic mapping, sidescan sonar, and SeaBeam comparison results, *Deep Sea Res., Part II*, *45*, 2547–2570.

Chadwick, W. W., D. S. Scheirer, R. W. Embley, and H. P. Johnson (2001), High-resolution bathymetric surveys using scanning sonars: Lavaflow morphology, hydrothermal vents, and geologic structure at recent eruption sites on the Juan de Fuca Ridge, *J. Geophys. Res.*, *106*, 16,075–16,099.

Clague, D. A., J. R. Reynolds, and A. S. Davis (2000), Near-ridge seamount chains in the northeastern Pacific Ocean, *J. Geophys. Res.*, *105*, 16,541–16,561.

Cormier, M.-H., W. B. F. Ryan, A. K. Shah, W. Jin, A. M. Bradley, and D. R. Yoerger (2003), Waxing and waning volcanism along the East Pacific Rise on a millennium time scale, *Geology*, *31*, 633–636.

Cotsonika, L. A., M. R. Perfit, D. S. Stakes, and W. I. Ridley (2005), The occurrence and origin of andesites and dacites from the southern Juan de Fuca Ridge, *Eos Trans. AGU*, *86*(18), Jt. Assem. Suppl, Abstract V13A-04.

Crawford, W. C., and S. C. Webb (2002), Variations in the distribution of magma in the lower crust and at the Moho beneath the East Pacific Rise at 9°–10°N, *Earth Planet. Sci. Lett.*, *203*, 117–130.

Denlinger, R. L. (1997), A dynamic balance between magma supply and eruption rate at Kilauea Volcano, Hawaii, *J. Geophys. Res.*, *102*, 18,091–18,100.

Dixon, J. E., D. A. Clague, and J.-P. Eissen (1986), Gabbroic xenoliths and host ferrobasalt from the southern Juan de Fuca Ridge, *J. Geophys. Res.*, *91*, 3795–3820.

Eaby, J., D. A. Clague, and J. R. Delaney (1984), Sr isotope variations along the Juan de Fuca Ridge, *J. Geophys. Res.*, *89*, 7883–7890.

Embley, R. W., and W. W. Chadwick (1994), Volcanic and hydrothermal processes associated with a recent phase of seafloor spreading at the northern Cleft segment: Juan de Fuca Ridge, *J. Geophys. Res.*, *99*, 4741–4760.

Embley, R. W., and D. S. Wilson (1992), Morphology of the Blanco Transform fault zone-NE Pacific: Implications for its tectonic evolution, *Mar. Geophys. Res.*, *14*, 25–45.

Embley, R. W., W. W. Chadwick, M. R. Perfit, and E. T. Baker (1991), Geology of the northern Cleft segment, Juan de Fuca Ridge: Recent lava flows, seafloor spreading, and the formation of megaplumes, *Geology*, *19*, 771–775.

Embley, R. W., W. W. Chadwick Jr., D. Clague, and D. Stakes (1999), 1998 eruption of Axial Volcano: Multibeam anomalies and sea-floor observations, *Geophys. Res. Lett.*, *26*(23), 3425–3428.

Fialko, Y. (2001), On the origin of near-axis volcanism and faulting at fast spreading mid-ocean ridges, *Earth Planet. Sci., Lett.*, *190*, 31–39.

Fornari, D. J., R. M. Haymon, M. R. Perfit, T. K. P. Gregg, and M. H. Edwards (1998), Geological characteristics and evolution of the axial zone on fast-spreading mid-ocean ridges: Formation of an axial summit trough along the EPR, 9°–10°N, *J. Geophys. Res.*, *103*, 9827–9855.

Fornari, D. J., et al (2004), Submarine lava flow emplacement at the East Pacific Rise 9°50′N: Implications for uppermost ocean crust stratigraphy and hydrothermal fluid circulation, in *Mid-Ocean Ridges: Hydrothermal Interactions Between the Lithosphere and Oceans*, *Geophys. Monogr. Ser.*, vol. 148, edited by C. R. German, J. Lin, and L. M. Parson, pp. 187–218, AGU, Washington, D. C.

Gripp, A. E., and R. G. Gordon (1990), Current plate velocities relative to the hotspots incorporation the NUVEL-1 global plate motion model, *Geophys. Res. Lett.*, *17*, 1109–1112.

Guspi, F. (1987), Frequency-domain reduction of potential field measurements to a horizontal plane, *Geoexploration*, *24*, 87–98.

Guyodo, Y., and J.-P. Valet (1999), Global changes in intensity of the Earth's magnetic field during the past 800 kyr, *Nature*, *399*, 249–252.

Haymon, R. M., D. J. Fornari, M. H. Edwards, S. Carbotte, D. Wright, and K. C. Macdonald (1991), Hydrothermal vent distribution along the East Pacific Rise crest (9°09′–54′N) and its relationship to magmatic and tectonic processes on fast-spreading mid-ocean ridges, *Earth Planet. Sci. Lett.*, *104*, 513–534.

Head, J. W., L. Wilson, and D. K. Smith (1996), Mid-ocean ridge eruptive vents: Evidence for dike widths, eruption rates, and evolution of eruptions from morphology and structure, *J. Geophys. Res.*, *101*, 28,265–28,280.

Hekinian, R., and D. Walker (1987), Diversity and spatial zonation of volcanic rocks from the East Pacific Rise near 21°N, *Contrib. Mineral. Petrol.*, *96*, 265–280.

Hooft, E. E., H. Schouten, and R. S. Detrick (1996), Constraining crustal emplacement processes from the variation in seismic layer 2A thickness at the East Pacific Rise, *Earth Planet. Sci. Lett.*, *142*, 289–309.

International Association of Geomagnetism and Aeronomy, Division V, Working Group 8, (2000), International Geomagnetic Reference Field 2000, *Geophys. J. Int.*, *141*, 259–262.

Juteau, T., D. Bideau, O. Dauteuil, G. Manach, D. D. Naidoo, P. Nehlig, H. Ondreas, M. A. Tivey, K. X. Whipple, and J. R. Delaney (1995), A submersible study in the western Blanco Fracture Zone, N.E. Pacific: Structure and evolution during the last 1.6 Ma, *Mar. Geophys. Res.*, *17*, 399–430.

Kappel, E. S., and W. B. Ryan (1986), Volcanic episodicity and a non-steady-state rift valley along northeast Pacific spreading centers: Evidence from SeaMARC I, *J. Geophys. Res.*, *91*, 13,925–13,940.

Karson, J. A. (2002), Geologic structure of the uppermost oceanic crust created at fast- to intermediate-rate spreading centers, *Annu. Rev. Earth Planet. Sci.*, *30*, 347–384.

Karson, J. A., M. A. Tivey, and J. R. Delaney (2002), Internal structure of uppermost oceanic crust along the western Blanco Transform Scarp: Implications for subaxial accretion and deformation at the Juan de Fuca Ridge, *J. Geophys. Res.*, *107*(B9), 2181, doi:10.1029/2000JB000051.

Lagabrielle, Y., and M.-H. Cormier (1999), Formation of large summit troughs along the East Pacific Rise as collapse calderas: An evolutionary model, *J. Geophys. Res.*, *104*, 12,971–12,988.

Macdonald, K. C. (1998), Linkages between faulting, volcanism, hydrothermal activity and segmentation on fast spreading centers, in *Faulting and Magmatism at Mid-Ocean Ridges*, *Geophys. Monogr. Ser.*, vol. 106, edited by W. R. Buck et al., pp. 27–58, AGU, Washington, D. C.

Macdonald, K. C., P. J. Fox, R. T. Alexander, R. Pockalny, and P. Gente (1996), Volcanic growth faults and the origin of Pacific abyssal hills, *Nature*, *380*, 125–129.

Maclennan, J., T. Hulme, and S. Singh (2005), Cooling the lower oceanic crust, *Geology*, *33*, 357–360.

MBARI Mapping Team (2001), *MBARI West Coast Seamounts and Ridges Multibeam Survey* [CD-ROM], *MBARI Digital Data Ser. 7*, Monterey Bay Aquarium Res. Inst., Moss Landing, Calif.

McElhinny, M. W., and W. E. Senanayake (1982), Variations in the geomagnetic dipole 1: The past 50,000 years, *J. Geomagn. Geoelectr.*, *34*, 39–51.

Normark, W. R., J. L. Morton, R. A. Koski, D. A. Clague, and J. R. Delaney (1983), Active hydrothermal vents and sulfide deposits on the southern Juan de Fuca Ridge, *Geology*, *11*, 158–163.

Normark, W. R., et al. (1986), Submarine fissure eruptions and hydrothermal vents on the southern Juan de Fuca Ridge: Preliminary observations from the submersible Alvin, *Geology*, *14*, 823–827.

Normark, W. R., J. L. Morton, and S. L. Ross (1987), Submersible observations along the southern Juan de Fuca Ridge: 1984 Alvin program, *J. Geophys. Res.*, *92*, 11,283–11,290.

Parker, R. L., and S. P. Huestis (1974), The inversion of magnetic anomalies in the presence of topography, *J. Geophys. Res.*, *79*, 1587–1594.

Perfit, M. R., and W. W. Chadwick (1998), Magmatism at mid-ocean ridges: Constraints from volcanological and geochemical investigations, in *Faulting and Magmatism at Mid-Ocean Ridges*, *Geophys. Monogr. Ser.*, vol. 106, edited by W. R. Buck et al., pp. 59–116, AGU, Washington, D. C.

Perfit, M. R., D. J. Fornari, M. C. Smith, J. F. Bender, C. H. Langmuir, and R. M. Haymon (1994), Small-scale spatial and temporal variations in mid-ocean ridge crest magmatic processes, *Geology*, *22*, 375–379.

Perfit, M. R., D. S. Stakes, M. A. Tivey, S. Kulp, W. I. Ridley, and T. M. Ramirez (2003), Magmagenesis and crustal formation of the southern Juan de Fuca Ridge (JdFR): Results of fine-scale sampling and mapping, *Geophys. Res. Abstr.*, *5*, EGS-AGU-EUG Jt. Assem., Nice, Abstract EAE03-A-07287.

Phipps Morgan, J., and Y. J. Chen (1993), The genesis of oceanic crust: Magma injection, hydrothermal circulation, and crustal flow, *J. Geophys. Res.*, *98*, 6283–6297.

Pollock, M. A., E. M. Klein, J. A. Karson, and M. A. Tivey (2005), Temporal and spatial variability in the composition of lavas exposed along the Western Blanco Transform Fault, *Geochem. Geophys. Geosyst.*, *6*, Q11009, doi:10.1029/2005GC001026.

Rubin, K. H., M. C. Smith, E. C. Bergmanis, M. R. Perfit, J. M. Sinton, and R. Batiza (2001), Geochemical heterogeneity of individual mid-ocean ridge lava flows: Insights into eruption, emplacement and global variations in magma generation, *Earth Planet. Sci. Lett.*, *188*, 349–367.

Scheirer, D. S., and K. C. Macdonald (1993), Variation in cross-sectional area of the axial ridge along the East Pacific Rise: Evidence for the magmatic budget of a fast-spreading center, *J. Geophys. Res.*, *98*, 7871–7885.

Schouten, H., M. A. Tivey, D. J. Fornari, and J. R. Cochran (1999), The central anomaly magnetic high: Constraints on volcanic construction of seismic layer 2A at a fast-spreading midocean ridge, the East Pacific Rise at 9°30–50′N, *Earth Planet. Sci. Lett.*, *169*, 37–50.

Sim, Y. (2004), Mechanics of complex hydraulic fractures in the Earth's crust, Ph.D. dissertation, Ga. Inst. of Technol., Atlanta.

Sim, Y., L. N. Germanovich, R. P. Lowell, and P. Ramondenc (2004), Diking magma lenses, and the location of hydrothermal sites at mid-ocean ridges, *Eos Trans. AGU*, *85*(47), Fall Meet. Suppl., Abstract B13A-0206.

Sinton, J. M., and R. S. Detrick (1992), Mid-ocean ridge magma chambers, *J. Geophys. Res.*, *97*, 197–216.

Sinton, J. M., D. S. Wilson, D. M. Christie, R. N. Hey, and J. R. Delaney (1983), Petrologic consequences of ridge propagation on oceanic spreading ridges, *Earth Planet. Sci. Lett.*, *62*, 193–207.

Sinton, J., E. Bergmanis, K. Rubin, R. Batiza, T. K. P. Gregg, K. Grönvold, K. C. Macdonald, and S. M. White (2002), Volcanic eruptions on mid-ocean ridges: New evidence from the superfast spreading East Pacific Rise, 17°–19°S, *J. Geophys. Res.*, *107*(B6), 2115, doi:10.1029/2000JB000090.

Smith, M. C. (1993), Petrologic and geochemical investigations of basalts from the southern Juan de Fuca Ridge, M.Sc. thesis, 192 pp., Univ. of Fla., Gainesville.

Smith, M. C. (1999), Geochemistry of eastern Pacific MORB: Implications for MORB petrogenesis and the nature of crustal accretion with the neovolcanic zone of two recently active ridge segments, Ph.D dissertation, 189 pp., Univ. of Fla., Gainesville.

Smith, M. C., M. R. Perfit, and I. R. Jonasson (1994), Petrology and geochemistry of basalts from the southern Juan de Fuca Ridge: Controls on the spatial and temporal evolution of mid-ocean ridge basalt, *J. Geophys. Res.*, *99*, 4787–4812.

Sohn, R. A., and K. W. W. Sims (2005), Bending as a mechanism for triggering off-axis volcanism on the East Pacific Rise, *Geology*, *33*, 93–96.

Soule, S. A., D. J. Fornari, M. R. Perfit, M. A. Tivey, W. I. Ridley, and H. Schouten (2005), Channelized lava flows at the East Pacific Rise crest 9°–10°N: The importance of off-axis lava transport in developing the architecture of young oceanic crust, *Geochem. Geophys. Geosyst.*, *6*, Q08005, doi:10.1029/2005GC000912.

Stakes, D. S., M. R. Perfit, M. A. Tivey, T. Walsh, M. McCann, T. M. Ramirez, and D. Caress (2003a), *Virtual Field Trip From the Juan de Fuca Ridge* [DVD], *MBARI Digital Data Ser. 8*, Monterey Bay Aquarium Res. Inst., Moss Landing, Calif.

Stakes, D., M. R. Perfit, C. G. Wheat, T. M. Ramirez, R. A. Koski, and J. Hein (2003b), Evidence of off-axis volcanism and hydrothermal venting along the Cleft segment of the southern Juan de Fuca Ridge, *Geophys. Res. Abstr.*, *5*, EGS/AGU/EUG Jt. Assem., Abstract EAE03-A-04666.

Tierney, S. E. (2003), Distribution and composition of lavas from the southern Cleft Segment of the Juan de Fuca Ridge: Tectonomagmatic evolution of a ridge-transform intersection, Masters thesis, Univ. of Florida, Gainesville.

Tivey, M. A., H. P. Johnson, C. Fleutelot, S. Hussenoeder, R. Lawrence, C. Waters, and B. Wooding (1998), Direct measurement of magnetic reversal polarity boundaries in a cross-section of oceanic crust, *Geophys. Res., Lett.*, *25*, 3631–3634.

Wilson, D. S. (1988), Tectonic history of the Juan de Fuca Ridge over the last 40 million years, *J. Geophys. Res.*, *93*, 11,863–11,876.

Wilson, D. S. (1992), Focused mantle upwelling beneath mid-ocean ridges: Evidence from seamount formation and isostatic compensation of topography, *Earth Planet. Sci. Lett.*, *113*, 41–55.

Wilson, D. S., R. N. Hey, and C. Nishimura (1984), Propagation as a mechanism of reorientation of the Juan de Fuca Ridge, *J. Geophys. Res.*, *89*, 9215–9225.